12-14-2016

Surface Charge Characterization of Anatase and Rutile using Flow Adsorption Microcalorimetry

Tyler Hawkins

SURFACE CHARGE CHARACTERIZATION OF ANATASE AND RUTILE USING FLOW ADSORPTION MICROCALORIMETRY

by

TYLER HAWKINS

Under the Direction of Dr. Nadine Kabengi PhD

ABSTRACT

Titanium dioxide (TiO_2) attracts extensive attention due to its widespread technological and environmental applications. This study seeks to investigate the surface charging behavior of the two TiO_2 polymorphs, anatase and rutile, using Flow Adsorption Microcalorimetry (FAMC). FAMC allows direct quantitative measurement of the heat of a surface reaction; these calorimetric heats are directly proportional to the surface charge. Determining the magnitude of positive and negative charges at the surface over a range of pHs allows for the determination of the point of zero net charge (PZNC) via a unique calorimetric method that removes many of the shortcomings related to the other analytical techniques used for such measurements.

INDEX WORDS: Surface charge, Ion-exchange, Heats of adsorption, TiO_2, Zero Point of Charge, Metal-oxide solution interface

SURFACE CHARGE CHARACTERIZATION OF ANATASE AND RUTILE USING FLOW ADSORPTION MICROCALORIMETRY

by

TYLER HAWKINS

A Thesis Submitted in Partial Fulfillment of the Requirements for the Degree of

Masters of Science

in the College of Arts and Sciences

Georgia State University

2016

SURFACE CHARGE CHARACTERIZATION OF ANATASE AND RUTILE USING FLOW ADSORPTION MICROCALORIMETRY

by

TYLER HAWKINS

Committee Chair: Nadine Kabengi

Committee: Daniel Deocampo

Kathryn Grant

Michael Machesky

David Wesolowski

Electronic Version Approved:

Office of Graduate Studies

College of Arts and Sciences

Georgia State University

December 2016

ACKNOWLEDGEMENTS

I thank my family and friends for their unwavering support and love. I would also like to thank the mentors that inspired and encouraged me along my academic journey. A special thanks to the mentor who cultivated my scientific curiosity at young age, my high school teacher Mrs. Robin Hoy, and to my advisor, Dr. Nadine Kabengi, for offering her knowledge and guidance during my studies. I am eternally grateful for those who made it possible for me to be where I am today. The SSA and electron microscopy work was supported by the Virginia Tech National Center for Earth and Environmental Nanotechnology Infrastructure (NanoEarth), a member of the National Nanotechnology Coordinated Infrastructure (NNCI), supported by NSF (ECCS 1542100). I would also like to thank all their staff.

TABLE OF CONTENTS

LIST OF TABLES

LIST OF FIGURES

1 INTRODUCTION

The interface between mineral surfaces and aqueous solutions plays an important role in numerous environmental and energy related applications. Metal-oxide (MO) minerals are of particular importance due to their natural abundance and wide range of surface reactivities (Vohs, 2013). In the presence of aqueous solutions, under-coordinated oxygen and metal ions at the MO surface react with water molecules in solution to form surface hydroxyl functional groups: ≡SOH (where ≡S represents a metal in the mineral structure and OH is the hydroxylated surface oxygen) (O'day, 1999). The protonation and deprotonation of surface hydroxyl groups in response to solution pH results in the formation of a net charge at the MO surface (Meyers, 1999). The pH dependent surface charge gives rise to an electrified region at the interface between the mineral and bulk solution, referred to as the electric double layer (EDL), where the condition of electronuetrality is achieved by the accumulation of counter-ions (ions of opposite charge to that of the surface) in a compact region near the surface and a diffuse region of counter- and co-ions (ions of the same charge to that of the surface) which decays to the bulk solution (Hunter, 1988). It is this retention (or release) of ions at MO/solution interface that has been the subject of interest in a wide variety of disciplines ranging from material science to geochemistry. MOs are employed as catalytic materials and used in the production of industrial chemicals and fuel cells often requiring ion adsorption processes from impregnation solutions (Rudzinski, 2000; Vohs, 2013). The adsorption or release of chemical species by charged MO surfaces plays a fundamental role in a number of geochemical processes including the mobility and fate of contaminants in subsurface environments (Smith, 1999). Some MOs exhibit large adsorption capacities for toxic heavy metals, organics, and/or oxyanions which make them ideal absorbents for remediation applications (Zhang et al., 2008). Optimization and development of these applications rely on the

ability to accurately model these interfacial systems. Increasing the accuracy of predictive models would provide immense benefits. For example, the models can better anticipate the movements of toxic heavy metals in groundwater environments and hence improve the technology implemented in the remediation efforts of these contaminants. Modeling MO/solution interfaces, which are fundamental to catalytic processes used in the majority of industrial applications, would cut time, energy, and cost when seeking to develop and improve production methods. Ultimately, the construction of comprehensive predictive models requires a mechanistic understanding of interfacial processes under a range of realistic conditions in which they occur (Kabengi et al., 2006).

Numerous experimental and computational methods have been applied to various MO/solution systems in order to investigate surface charge development and ion adsorption processes. The results of these investigations are typically understood using surface complexation models (SCMs), which are founded on chemical and electrostatic descriptions of the EDL (O'Day, 1999). Although SCMs have proven to be useful for understanding macroscopic adsorption data, they demand an extensive amount of parameters to constrain their complexities (Goldberg, 2014). Many of these parameters are not perfectly known and are often adjusted to fit experimental data, "thus it may not be surprising that equilibrium data will fit a number of the models equally well (Sparks, 2001)." Acquiring as many realistic modeling inputs as experimentally possible over a range of MO-solution interfaces and in a variety of conditions is necessary to accurately parameterize surface complexation models, as well as to provide a point of reference for quantum calculations that are essential in computational methods targeted to improve model accuracy. Constructing comprehensive predictive models of these interfacial systems requires collecting data from many different experimental techniques (Fenter et al., 2000).

1.1 Metal Oxide-Solution Systems

Surface Charge

As mentioned above, the formation of net charge on the MO surfaces results from the protonation and/or deprotonation of surface hydroxyl groups in response to solution pH. The mechanisms of charge development can be described by surface ionization models, including the two-pK model where the surface functional group, ≡SOH, undergoes protonation (Eq. 1) and deprotonation (Eq. 2):

$$\equiv \mathrm{SOH} + \mathrm{H}^{+} \leftrightarrow \equiv \mathrm{SOH}_{2}^{+} \quad [1]$$

$$\equiv \mathrm{SOH} \leftrightarrow \equiv \mathrm{SO}^{-} + \mathrm{H}^{+} \quad [2]$$

Other models include the one-pK model, based on the concept that each surface site undergoes only one protonation reaction

$$\equiv \mathrm{SOH}^{\frac{1}{2}-} + \mathrm{H}^{+} \leftrightarrow \equiv \mathrm{SOH}_{2}^{\frac{1}{2}+} \quad [3]$$

The multisite complexation model (MUSIC) model identifies different sites based on crystal structure such that various types of surface hydroxyl groups can exist on MO surfaces (Hiemstra et al., 1996). According to the MUSIC model, the type(s) of surface groups depends on the number of coordinating structural metal ions (i.e. ≡S). For example, oxygen or OH species may be coordinated to one, two, or three structural metal atoms (denoted as singly, doubly, or triply coordinated surface hydroxyl groups, respectively) and will consequently exhibit different chemical reactivities (Hiemstra et al., 1989; Hiemstra and VanRiemsdijk, 1999; Sparks, 2003).

The number of hydroxyl groups that can potentially protonate (or deprotonate) and the degree to which they react with protons is a function of the valence and coordination of the metal cation in the mineral structure (Essington, 2011). In other words, the pH dependent surface charge generated from the adsorption of H^+ or OH^- , termed potentially-determining ions, is a surface charge characteristic that is intrinsic to the mineral itself (Sposito, 2008).This pH-dependent charge, often referred to as the net proton density charge, σ_H, is net positive under acidic conditions due to the uptake of protons by surface functional groups and is net negative in basic conditions owing to the release of protons by surface groups (Goldberg, 2007). Any deficit or excess of charge present at the surface is neutralized by the distribution of ions in the interfacial region between the solid and bulk liquid phases giving rise to the EDL (Sparks, 2003).

1.1.2 *The Electric Double Layer*

Figure 1.1 depicts a simplified schematic of the EDL which is generally considered to include at least one compact (Stern) layer of concentrated counter-ions located closest to the surface and a diffuse layer further out from the interface of counter- and co-ions whose concentrations decrease exponentially from the surface out into the bulk solution (Fenter, 2000; Wesolowski, 2008).

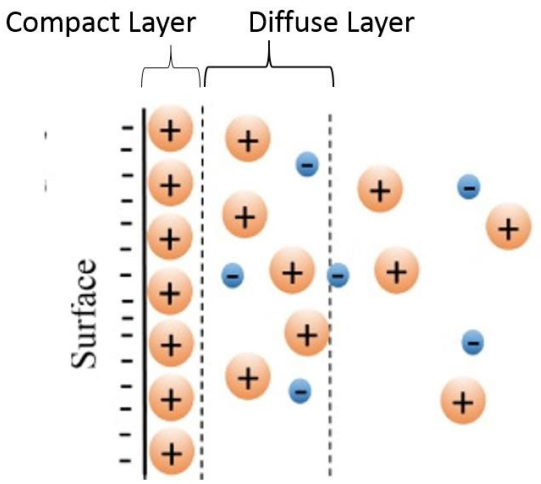

Figure 1.1. Simplified schematic of the Electric Double Layer (EDL) (modified from Kenichi et al., 2015).

The accumulation of counter-ions near the surface generates an excess electrical potential which also decreases with distance from the surface until it becomes zero in the bulk solution (Hunter, 1981). The distribution of charge within the EDL, i.e. the distribution of the electric potential, is dependent on the magnitude of the surface charge (Hunter, 1981).

1.1.3

Ion Adsorption

Ions in solution can be retained at the interface through different mechanisms such as inner-sphere complexation, outer sphere complexation, or retention in the diffuse swarm (Essington, 2011). If a surface functional group reacts with an ion in solution to form a stable molecular unit (a surface complex) the reaction is termed surface complexation (Sposito, 2008). Inner- sphere complexes form when ions bind directly to surface functional groups such that no water molecules exist between them (Sparks, 2003). Outer-sphere complexes form where ions retain some or all of their hydration waters and electrostatically bind to surface functional groups (Sparks, 2003). The electrostatic retention of ions not bound as surface complexes, but that are nonetheless associated

with the surface, are said to be adsorbed in a delocalized sense in the diffuse ion "swarm" (Sposito, 2008). These ions are freely mobile but hover near the surface to balance any excess surface charge contributed by the mineral structure (σ_H) and by immobilized ions adsorbed as surface complexes (σ_{is} and σ_{os}):

$$\sigma_H + \sigma_{is} + \sigma_{os} + \sigma_d = 0 \quad [4]$$

where, σ_H is net proton charge, σ_{is} and σ_{os} refer to the net charge of ions adsorbed in inner-sphere (σ_{is}) and outer-sphere complexes (σ_{os}), respectively, and σ_d is the charge of counter ions retained in the diffuse ion swarm needed to achieve surface charge balance (Essington, 2011; Sparks, 2003; Sposito, 2008). Inner-sphere complexes involve strong ionic and/or covalent bonding and thus are said to be "specifically" adsorbed. (Smith, 1999). Outer-sphere complexation and diffuse ion screening involve weaker electrostatic mechanisms and are said to be "non-specifically" adsorbed, making them less stable than inner-sphere complexes and more readily exchangeable (Essington, 2011). In acidic pH conditions, the net positive surface charge results in the attraction of anions in solution, whereas in basic conditions the net negative surface charge attracts cations (Cheng, 2014).

1.1.4

Points of Zero Charge

There exists several pH values associated with specific conditions imposed on one or more of the surface charge densities defined above (Eq. 4). These are termed the points of zero charge whereby for example, the point of zero net proton charge (PZNPC) is the pH at which σ_H is equal to zero and the point of zero salt effect (PZSE) is the pH at which ($\delta\sigma_H / \delta I$) is zero (Sposito, 1981). It is not uncommon, under specific experimental conditions (for e.g. 1:1 electrolytes, low ionic strengths) to achieve equality between 2 or more points of zero charge conditions. For instance, the PZSE = PZNPC if the only specifically adsorbed species are the potentially determining ions,

H^+ and OH^- (Appel et al., 2002).

There exists a pH, referred to as the point of zero charge (PZC), where the charge changes sign, such that the sum of the positive surface charge balances the sum of all the negative surface charge (Marcano-Martinez, 1989). The PZC is a reflection of the bulk mineral structure and considered an important characteristic feature of mineral surfaces (O'Day, 1999).

The ability to accurately model the metal-oxide solution systems relies on understanding the pH-dependent charge development of MO surfaces, and the accompanying arrangement of ions at MO-solution interfaces. The mechanisms of protonation/deportation of surface functional groups, electrostatic parameters and descriptions of the EDL, ion adsorption mechanisms (IS, OS, or diffuse screening) and the points of zero charge are just some examples of the data and equations used to parametrize SCMs.

1.1.5 *Surface Complexation Models*

Representing adsorption with empirical approaches (adsorption isotherms) results in over simplified and purely descriptive models that are not predictive beyond the conditions at which they were measured because they are not able to account for effects of variable chemical conditions (pH, ionic strength, etc.) on adsorption reactions (Goldberg, 2007). The most widely accepted models used to describe pH and ionic strength dependent charge development (and thus ion adsorption), are the site-binding electrostatic models known as surface complexation (SCM) models (Tombácz, 2009). SCMs are "chemical models that are based on molecular descriptions of the EDL using equilibrium-based adsorption data (Goldberg, 1992)." SCMs can describe adsorption on mineral and soil surfaces over a range of geochemical conditions because they are mechanistic models which can account for the effects of variable chemical conditions by directly describing aqueous and surface speciation and distribution (Zheng and Selim, 2013). SCMs

generally have the following in common: an adsorption model which identifies the type(s) and reactivity of surface sites and an electrostatic model of the EDL that describes the distribution of ions in one or more planes adjacent to the surface and identifies the relationship between charge and potential for each plane (Tadanier and Eick, 2002). Differences in SCMs lie in their descriptions of the EDL such as the number of planes in the interface and location of complexes in relation to the mineral surface (Sposito, 1984). A few common SCMs (Basic Stern, Triple Layer Model, and CD-MUSIC) are described below.

The Basic Stern (BS) model depicts the interface with two layers, the compact and diffuse, where the compact layer is divided into two charged regions: the 0-plane (containing surface hydroxyl groups) and 1-plane (outer Helmholtz plane (OHP)) marking the start of the diffuse layer (Bourikas et al., 2014). Counter ions at the OHP are considered weakly bound outer sphere complexes (Tombácz, 2009). Ions in this model are restricted from approaching the surface too closely due to both their hydration shell layers and layers of water adsorbed at the surface (Bourikas et al., 2014). This results in an uncharged layer which sits between the 0-plane and 1-plane. This impels the layer to behave as a plate capacitor, with a given capacitance, C, that is related to the distance between the 0- and 1-plane, *d*, by the equation:

$$C = \varepsilon_0 \varepsilon_r / d$$

Where ε_0 is the dielectric constant of the uncharged layer and ε_r is the mean relative dielectric constant of the layer. The dielectric constant is an expression of the ability of a substance to store electrical energy in an electric field (Brown et al., 1999).

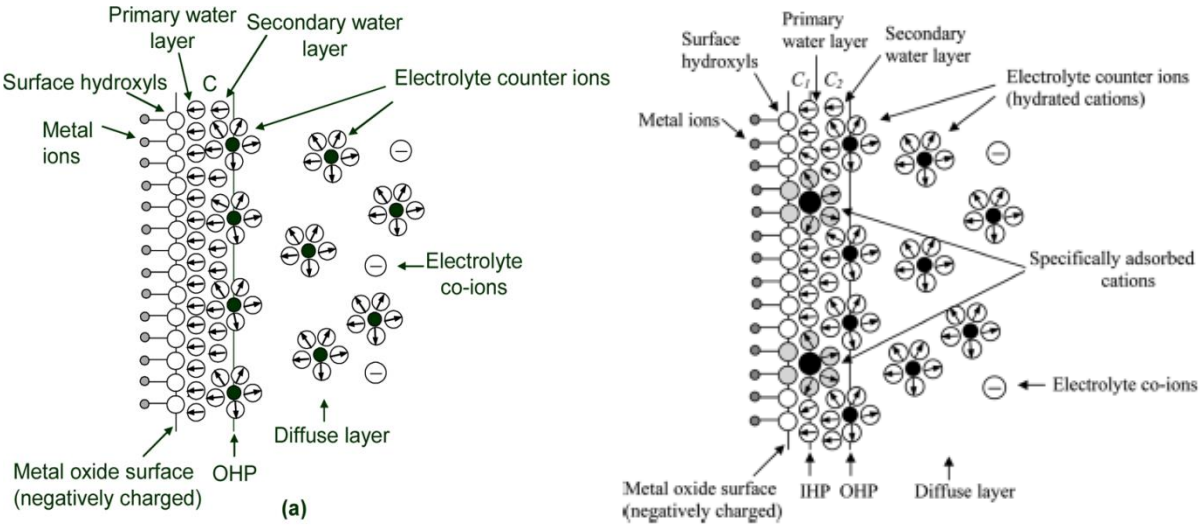

Figure 1.2. Basic Stern (BS) model (left) and Triple Layer Model (TLM) (right) (Modified from Bourikas et al., 2014).

The Triple Layer Model (TLM) differs from the BS model only by the addition of the inner Helmhotz plane (IHP) between the surface and the OHP. Inner-sphere complexes are considered to be located in the IHP, now considered plane 1, and outer sphere complexes in the OHP, now plane 2 (Guichet, 2006). Figure 1.2 depicts the division of the interface into three layers, the surface-IHP, IHP-OHP, and the diffuse layer, of the TLM (Bourikas, 2014). The surface-IHP and IHP-OHP layers are considered to have separate capacitance values which are related to the total capacitance by:

$$1/C = 1/C_1 + 1/C_2$$

where, C_1 and C_2 represents the capacitance values of layers 1 and 2, respectively (Bourikas et al., 2014).

The Charge Distribution Multi-Site Surface Complexation (CD-MUSIC) model is one of the more modern and realistic models commonly used today. The CD-MUSIC model accounts

for the specific types of oxygen atoms known to exist from structural analysis data (Hiemstra et al., 1996; Bourikas et al., 2014). The model employs the concept of charge neutralization of an oxygen by a metal ion based on the *actual bond valence* to predict the proton affinity of individual surface groups (Hiemstra, 1996). Bond valence (v) is defined as the charge of the metal ion (z) divided by its coordination number (CN):

$$v = \frac{z}{CN}$$

This is used to calculate the excess charge of surface oxygens by the sum of its charge (z = -2) plus the bond valances of all coordinated metal ions and the number of proton accepting and donating hydrogen bonds (Σv_m):

$$\text{surface oxygen charge} = z + \Sigma v_m$$

Oxygens coordinated to different numbers of metal ions will have different charge values. Combining this description of surface protonation with the distribution of charge for adsorbed ions between surface and Stern planes results in the CD-MUSIC model. CD-The MUSIC model provides one of the more realistic molecular scale representations of the complex processes occurring at the MO-solution interface.

The mechanistic approach taken by SCMs makes them more flexible in their application to geochemical processes than most empirical models (Goldberg, 2007). However, in order to specify adsorption mechanisms and define specific surface complexes for all adsorbing ions, SCMs require an extensive amount of parameters to constrain their complexities and many of these parameters are not perfectly known (Goldberg, 2014). Thus, SCMs are often "poorly constrained, and the electrostatic parameters and equilibrium constants may be highly covariant (Ridley, 2009)." This can lead to the use of multiple adjustable parameters being employed to fit

experimental data, resulting in a number of models that fit equilibrium data equally well (Sparks, 2001). For example, Westall and Hohl (1980) applied acid-base titration data on TiO_2 and γ-Al_2O_3 to the Constant Capacitance Model (CCM) and TLM and found that each model fits the data reasonably well and thus concluded that one model was about as good as another (Westel and Hohl, 1980). However, just because good fitting can be accomplished it does not mean the model provides any realistic or relevant insight into the processes taking place (Tombacz, 2009). To improve predictive capabilities of SCMs and minimize the amount of adjustable parameters, it is important to determine as many realistic modeling inputs as experimentally possible over a range of MO-water interfaces and under a variety of conditions (Machesky, 2015). Data from a variety of experimental methods and improvements in molecular modeling simulations and quantum mechanics calculations will continue to provide the macroscopic and molecular scale information on which to build more effective and realistic SCMs (Machesky, 2015).

Various electrochemical and spectroscopic techniques have been applied to investigate the MO/electrolyte solution interface (Kallay 2010). Microscopic scale evidence of ion adsorption mechanisms can be obtained from direct experimental methods including spectroscopic and scattering techniques (Goldberg, 2014). For example, X-ray absorption spectroscopy (XAS) can be used to determine structural information of absorbed ions such as whether an ion is bound in an inner-sphere or outer-sphere complex as well as the denticity of the complex (Goldberg, 2014). This type of micro scale structural information is used to help constrain SCMs.

Ion adsorption mechanism and surface charge can also be determined from indirect macroscopic information from PZC shifts and ionic strength dependence experiments (Goldberg, 2014). Electrophoretic mobility titrations measure the movement of charged particles in solution when an electric field is applied (McFadyen, 1993). Zero mobility indicates the zero net surface

charge known as the isoelectric point (IEP) (Kosmulski, 2009). The PZC will shift if specific adsorption of ions in inner-sphere complexes occurs (Hunter, 1981). Potentiometric titration involves obtaining titration curves at various ionic strengths. When the titration curves are plotted together a common intersection point indicates the PZSE. The PZSE is the pH where the charge densities of potentially determining ions (H^+ and OH^-) are independent of ionic strength (Appel, 2002). It is common for studies to incorporate a number of these techniques to achieve the maximum amount of molecular and macroscopic data possible in order to successfully apply SCMs. Wesolowski et al. (2008) successfully described cation adsorption data from pH titrations of rutile with the Gouy-Chapman Stern model constrained using the inner-sphere binding mechanisms observed from X-ray studies and computational modeling.

The equations used to parameterize SCMs, acquired from surface protonation and ion adsorption experiments for a given solid may differ for several reasons. This can be seen in the range of PZC values tabulated of numerous MOs, from both theoretical calculations and experimental measurements. The differences results from the surface neutral condition being defined as PZC, i.e. the type of point of zero charge, as well as the experiment used to determine it (Davis and Kent, 1990; O'Day, 1999; Kosmulksi, 2002; Sverjensky, 2005). For example, the pH of the PZSE is the intersection point of surface titration curves obtained at different ionic strengths, which for some solids can be dependent on ionic strength and electrolyte type used in the experiments. Thus the pH of PZSE may not equal the PZC (Lützenkirchen, 1998). The isoelectric point (IEP) determined at low ionic strengths from electrokinetic experiments is considered to be more representative of the PZC than the pH_{PZSE} (Lützenkirchen, 2012). However, at low surface charge, the movement of the particle under the influence of the electric field may be retarded and hence the IEP may also misrepresent the PZC.

Differences in measured SCM parameters can arise, even for a given solid using the same experimental technique, if employing different electrolyte solutions. Ion adsorption equilibrium constants have been predicted to vary for different electrolyte ions and solids. For example, the expected equilibrium constants of any particular cation decrease with decreasing dielectric constant of the solid, imparting greatly different behaviors for solids with low and high dielectric constants (Sverjensky, 2005). Equilibrium constants of the high dielectric constant solids, such as rutile (TiO_2; $\varepsilon_k = 114$), decrease with increasing cation size in the sequence $Li^+ > Na^+ > K^+ > Rb^+$ and Cs^+, whereas low dielectric constant solids such as quartz ($\varepsilon_k = 4.6$) follow the opposite trend (Sverjensky, 2005). For a given high (or low) dielectric solid the difference in ion adsorption equilibrium constants result in differences in surface charge depending on the identity of the electrolyte utilized in the experiment. However, intermediate dielectric constant solids are not known to demonstrate an ion binding preference; ions typically adsorb on these solids to a similar degree (Sverjensky, 2005). The other major TiO_2 polymorph, anatase, is considered an intermediate dielectric constant solid (anatase: $\varepsilon_k = 18.6$). Thus, the two TiO_2 phases should theoretically have very different charging behaviors. In this study, the development of surface charge was investigated on the high ε_k solid, rutile, and the intermediate dielectric constant solid, anatase. It should be expected that the above cation selectivity series will be followed for rutile while anatase should not show any significant cation affinity.

1.2 Titanium Dioxide

The use of TiO_2 in technological applications has continued to increase in recent years due to its natural abundance, low toxicity, chemical stability, and most notably its photocatalytic properties. TiO_2 nanoparticles are drawing significant attention as photocatalysts used in the remediation of organic contaminants (Wypch, 2014). Understanding the charging behavior of TiO_2

is critical for making accurate predictions about its behavior under various conditions to facilitate its use in industrial and environmental applications. As mentioned above the two major polymorphs of TiO_2 are rutile and anatase. Anatase is largely considered to exhibit higher photocatalytic activity compared to rutile because of its higher specific surface area and hence reactivity.

Anatase and Rutile

Both anatase and rutile crystals are formed by chains of distorted TiO_6 octahedra (CN=6)

1.2.1

(Figure 1. 3a). The tetragonal structure of anatase (Fig. 1.3b) contains four TiO_2 units while the tetragonal structure of rutile (1.3.c) conventionally contains two TiO_2 units in its unit cell.

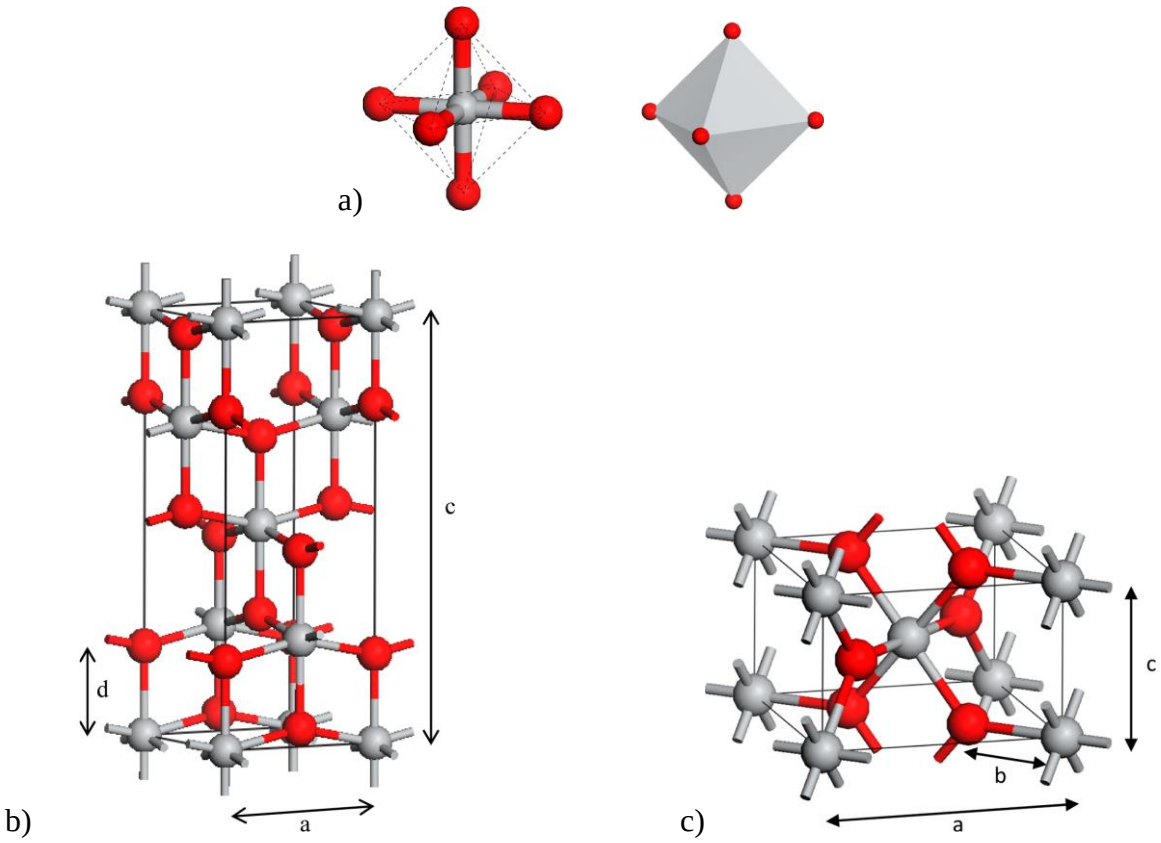

Figure 1.3. Bulk structure of anatase and rutile. Ti atoms (grey) are coordinated to six oxygen atoms (red): (a) Distorted TiO_6 octahedron of anatase and rutile, (b) Tetragonal structure of anatase, and (c) Tetragonal structure of rutile.

It is the stacking of the octahedra in the bulk structure that differentiate the two polymorphs (Fig. 1.4). In the anatase structure, each octahedron is in contact with eight neighboring octahedra linked by four common edges, while in the rutile structure each octahedron is in contact with 10 neighboring octahedron where two common edges are shared (Hiemstra, 1996).

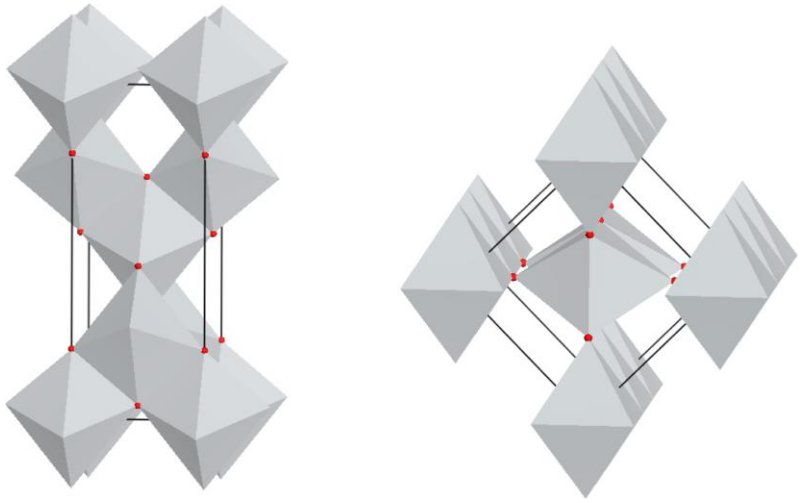

Figure 1.4. Bulk structure of anatase (left) and rutile (right).

The structural oxygen atom in both anatase and rutile is coordinated to three titanium atom, $\equiv Ti_3O^o$, by a long (apical) and two short bonds (equatorial).

1.2.2

Surface Charge and Ion Adsorption

According to the MUSIC model, the oxygen atoms receive a bond valence of +2/3 from the Ti atom. The mineral surfaces of TiO_2 can have three surface hydroxyl groups, i.e. singly, doubly, and triply coordinated. Hiemstra (1996) applied the bond valence approach in the MUSIC model to anatase and rutile and calculated the affinity of the different types of surface groups on the faces of rutile and anatase shown in table 1.1 and 1.2, respectively.

Table 1.1. Affinity Constants for Rutile Calculated with the MUSIC Model (Hiemstra, 1996)

Group	N_s (nm^{-2})	$\log K_{oxo}$	$\log K_{hydroxo}$	Charge $\Sigma s_j + V$ (oxo)	Charge $\Sigma s_j + V$ (hydroxo)	Crystal face index
≡TiO(a)	8.0	18.0	*+6.1*	-0.91	*-0.31*	101
≡TiO(a)	5.2 and 7.4	19.4	*+7.5*	-0.98	*-0.38*	110 and 100
$\equiv Ti_2O$(ab)	8.0	*+5.8*	-6.1	*-0.29*	+0.31	101
$\equiv Ti_2O$(2a)	5.2 and 7.4	*+4.4*	-7.5	*-0.22*	+0.38	110 and 100
$\equiv Ti_3O$(a)	-	*-4.0*	-	*+0.20*	-	110

≡TiO (a and b), two types of singly coordinated groups based on short (a) and long (b) Ti-O bond distances.
$\equiv Ti_2O$ (2a and ab), two types of doubly coordinated groups having a combination of short (a) and long (b) Ti-O bond distance (ab) or two short distances (2a).
N_s, site density in nm^{-2}.

Table 1.2. Affinity Constants for Anatase Calculated with the MUSIC Model (Hiemstra, 1996)

Group	N_s (nm^{-2})	$\log K_{oxo}$	$\log K_{hydroxo}$	Charge $\Sigma s_j + V$ (oxo)	Charge $\Sigma s_j + V$ (hydroxo)	Crystal face index
≡TiO(a)	5.6 and 5.2	18.2	*+6.3*	-0.92	*-0.32*	010 and 011
≡TiO(a)	7.0	19.1	*+7.2*	-0.97	*-0.37*	001
$\equiv Ti_2O$(ab)	5.6 and 5.2	*+5.6*	-6.3	*-0.28*	+0.32	010 and 011
$\equiv Ti_2O$(2a)	7.0	*+4.7*	-7.2	*-0.23*	+0.37	001
$\equiv Ti_3O$(a)	-	*-4.0*	-	+0.20	-	All

≡TiO (a and b), two types of singly coordinated groups based on short (a) and long (b) Ti-O bond distances..
$\equiv Ti_2O$ (2a and ab), two types of doubly coordinated groups having a combination of short (a) and long (b) Ti-O bond distance (ab) or two short distances (2a).

The (110) (Figure 1.5 top left) and (101) (Figure 1.5 bottom left) are the dominant and most stable faces on rutile and anatase, respectively.

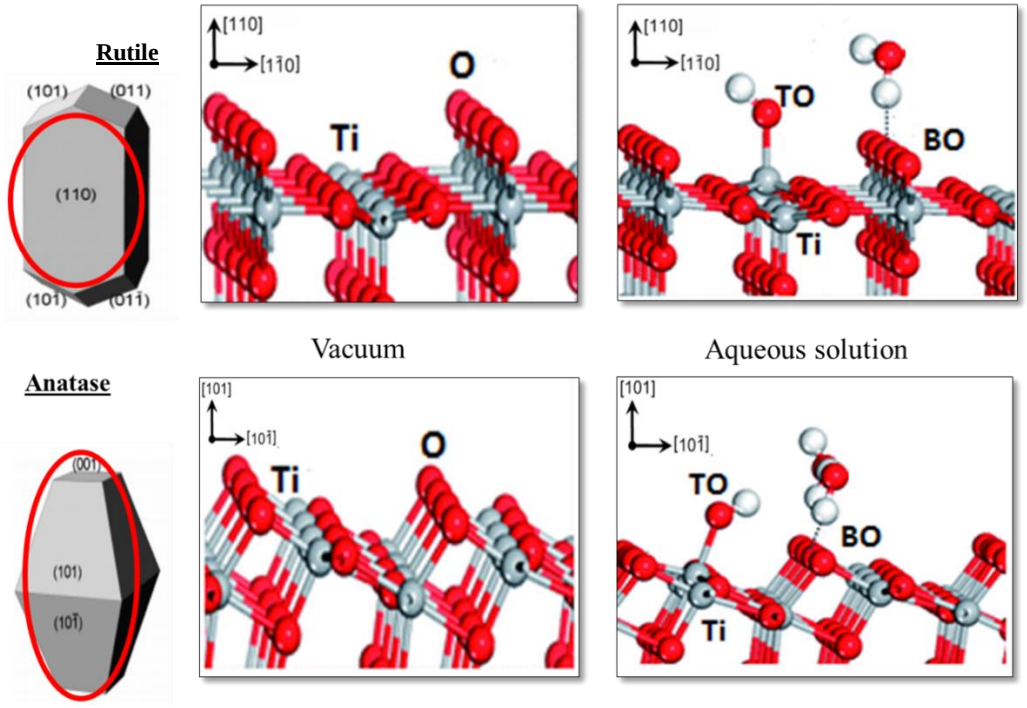

Figure 1.5. Crystal morphology of Rutile (top left) and Anatase (bottom left). Circles are drawn to indicate the dominant face. Atomic surface structure for a clean surface of the dominant (110) face for rutile (top middle) and (101) face for anatase (bottom middle). Atomic surface structure for dissociated water states on dominant surfaces in aqueous solution for rutile (top right) and anatase (bottom right). Grey represents titania atoms and red oxygen atoms. TO, refers to the terminal oxygen, bonded to one underlying Ti atom and BO, the bridging oxygen, bonded to two underlying Ti atoms.

Most surface and interfacial chemistry studies have focused on the (110) rutile face while the (101) face on anatase receives much less attention (Bandura, 2004; Bourikas, 2014; Brown, 1999; Machesky, 2006; Predota, 2004; Zhang, 2004). Figure 1.5 depicts the dissociated water of surface groups on the dominant faces of rutile (top right) and anatase (bottom right). Oxygen atoms bonded to one underlying Ti atom are termed terminal oxygens (TO) and oxygen atoms bound to two underlying Ti atoms are referred to as bridging oxygens (BO). Panagiotou (2008) investigated the charging behavior of a titania sample (containing anatase (80% w/w) and rutile (20% w/w)) by using potentiometric titrations data (over a wide range of pH), electrophoretic mobility

measurements, and streaming potential measurements along with ab initio calculations. By applying the "three plane" model to estimate the charge on Ti and O atoms at various exposed faces, maps of TiO(H) and $Ti_2O(H)$ surface groups at various ionic strength were obtained. Figure 1.6 illustrates the map obtained at 0.1 M ionic strength.

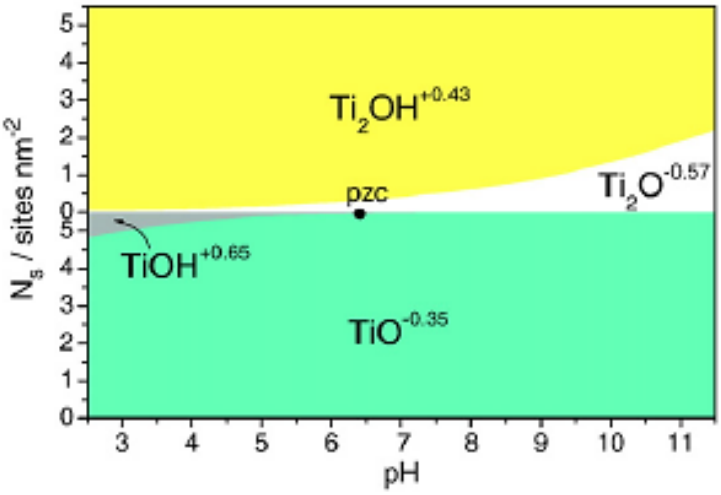

Figure 1.6. A map of of titania surface groups at 0.1 M ionic strength (modified from Panagiotou, 2008).

At pHs > than pzc practically all TO (i.e. TiO) groups are nonprotonated (represented in green in Figure 1.6). The nonprotonated TO groups also dominate at pHs < than the PZC, although a small fraction of protonated TOs appears at pHs lower than 5 (shown in grey on Figure 1.6). At low pHs, the majority of BO (i.e. Ti_2O) groups are protonated (shaded yellow in Figure 1.6), although a small portion of the BO groups start to deprotonate around pH 5 and this continues with increasing pH (shown in white in Figure 1.6).

1.3 Flow Adsorption MicroCalorimetry

Instrumentation and Operation

Flow microcalorimetry (FAMC) allows direct, continuous, and quantitative measurement of the heat of a reaction. FAMC is an ideal method for investigating interfacial interactions and 1.3.1 has been used to investigate the surface reactivity of a number of MOs (Kabengi, 2006; Rhue, 2002; Schneider, 1997). FAMC can be used in conjunction with other techniques to uncover information about surface reactions and charging behavior that cannot be easily acquired by conventional methods. The flow microcalorimeter consists of a column packed with a known amount of solid material (between 1 to 50 mg). An electrolyte solution flows through the column until thermal equilibrium is reached; producing a steady baseline. The input solution is changed to one of different composition (or pH, ionic strength, etc.). The new chemical solution reacts with the solid producing a change in the temperature of the solution flowing through the column. A pair of thermistors, one upstream and one downstream from the solid, form one half of an electronic bridge and sense temperature changes in the solution as it passes through the column. The change in solution temperature produces a differential output voltage from the bridge which, when amplified, is plotted as a function of time. Figure 1.7 shows a schematic of the FAMC set up.

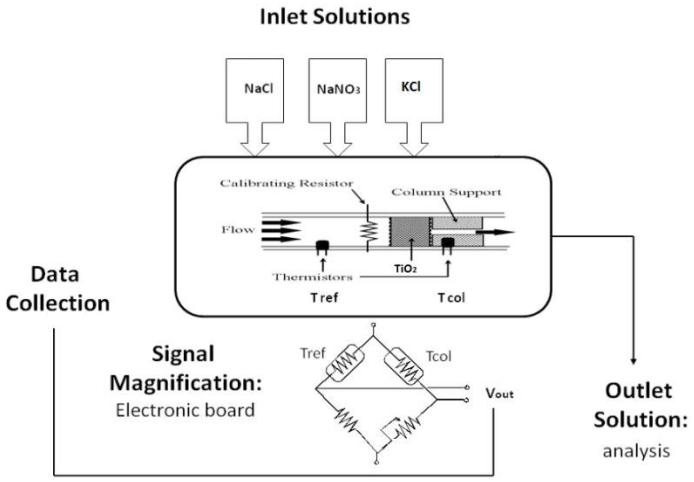

Figure 1.7 Schematic of the Flow Adsorption Microcalorimeter (FAMC).

Data Interpretation

1.3.2

A calibration heat pulse of known energy is given and recorded. Peak areas of the exchange reactions are obtained by integrating the signal over time and are converted to energy units by comparing with the calibration heat pulses. Five different input lines merge at a central manifold connected to the column containing the solid. The solid can be exposed to any order of different chemistries. The calorimeters operate in either continuous or pulse-injection mode and possess high sensitivity, low thermal drift, good signal-to-noise ratios and can detect temperature changes on the order of $10^{-5} – 10^{-6}$ °C.

1.4 Objectives

The overall objectives of this research was to investigate the charging development on TiO_2 polymorphs, anatase and rutile, and to probe the interface using the heats of ion exchange to provide experimental data needed to improve predictive modeling efforts. This overall goal was achieved by undertaking the following specific objectives:

1. Compare surface charge development on both anatase and rutile.
2. Probe the differences in surface reactivity for each polymorph at various pH conditions and hence obtain the PZNC defined in this experiment as the pH where the total negative charge equals the total positive charge.
3. Investigate the effect of different ion pair exchanges on charge development on rutile.

2 MATERIALS AND METHODS

2.1 Chemical Reagents

All chemicals used in the experiment were ACS reagent grade and were used as received from Fisher Scientific (Fairlawn, NJ). Solutions of 50 mM NaCl, $NaNO_3$, KCl, KNO_3, and RbCl were prepared using 18.2 MΩ deionized water. Solutions were adjusted to desired pHs using one of the following acids as appropriate to the particular experimental protocol: 5 M HCl, HNO_3, NaOH, KOH, and RbOH.

2.2 Mineral Phases

The anastase used in this experiment was obtained from Ishikhara Techno Corporation (Osaka, Japan) in nanometer powder form with the designated name ST-01(Ridely et al., 2006). The rutile sample was obtained from Tioxide Specialties Ltd. (Cleveland, UK) (Machesky et al., 1994). Prior to being used, both samples were subjected to multiple washing-centrifuging cycles in deionized water to reduce the presence of impurities. The N_2-BET specific surface area (SSA) of both samples was determined by the Brunauer-Emmet-Teller N_2-BET gas adsorption isotherm method. The SSAs of the anatase and rutile samples were 306.7 m^2/g and 17.0 m^2/g, respectively.

2.3 Flow Adsorption Microcalorimeter

The flow adsorption microcalorimeter in this study is comprised of a glass micro-column sealed inside an airtight vessel submerged in 50 L of water and maintained at room temperature. A calibrating resistor and two thermistors are attached to the glass micro-column. The sample was packed into the column and an electrolyte solution was passed through the assembly at a flow rate between 0.25 and 0.35 mL/min. One thermistor, located upstream from the solid, sensed the temperature of the incoming solution. The other thermistor, located downstream from the solid, sensed the temperature of the solution after interacting with the sample. The electrolyte solution

was passed through the column at a constant flow rate until a steady baseline was achieved. Then, the composition of the input solution was changed as dictated by the experimental protocol. The pair of thermistors detected the accompanying temperature changes in solution as it was passed through the column and interacted with the packed solids. The change in temperature produced a differential output voltage, which was amplified and sent to a computer for processing. The signal was measured every 5.0 s and plotted against time. The area of each calorimetric peak was obtained by integrating the signal over time using Graph Utility, a data processing software custom designed for FAMC data collected in the Kabengi laboratory. Peak areas were converted to energy units (mJ) by comparison with peak areas generated from calibration heat pulses of known energy obtained by energizing the calibrating resistor at a known current, voltage, flow rate and time.

2.4 Heats of Ion Exchange

Experiments were conducted using a known mass (approximately 40 mg) of solid, either anatase or rutile, packed into the column. Anions, Cl^- and NO_3^-, were used to probe the positive surface charge, whereby the sample was initially saturated with 50 mM NaCl solution until a steady baseline was achieved. The input solution was switched to 50 mM $NaNO_3$ and the heat of exchange generated from the displacement of Cl^- by NO_3^- , hereafter referred to as C/**N**, was recorded. Once the signal returned to baseline, the input solution was changed back to 50 mM NaCl, and the peak produced from the heat of the displacement of NO_3^- by Cl^-, referred to as N/**C**, was recorded. The exchange of C/**N** produced an exothermic heat signal while N/**C** generated an endothermic signal. The process of obtaining one C/**N** and one N/**C** exchange constituted one exchange cycle. Several (4-10) cycles were carried out. The peak areas of the C/**N** exotherms and N/**C** endotherms were averaged separately and subsequently used to calculate the heat of the ion exchange reactions (in mJ/mg). Cations, Na^+ and K^+, were used to probe the positive surface charge in a similar fashion.

Heats of exchange were obtained by changing between 50 mM NaCl and 50 mM KCl solutions. Table 1.3 lists the abbreviations and calorimetric signals for each ion exchange.

Table 2.3 Ion Exchange Abbreviations

Surface Charge Probed by Exchange	Y/**X**	Ion (Y±) on the surface/ exchanged with ion (**X±**) in solution		Sign of Calorimetric Signal
Positive	N/**C**	NO_3^-	Cl^-	(+) Endothermic
	C/**N**	Cl^-	NO_3^-	(-) Exothermic
Negative	K/**Na**	K^+	Na^+	(+) Endothermic
	Na/**K**	Na^+	K^+	(-) Exothermic

2.4.1 *Point of Zero Net Charge Determination*

The heats of Cl^- and NO_3^- exchanges and K^+ and Na^+ exchanges were measured using the procedure above with solutions at pH 3.25, 5.8 and 11.0. First, the experiment was run with unbuffered solutions with a pH value of about 5.8. After 5-10 acceptable cycles were recorded, the experiment was repeated at pH 3.25, where NaCl and KCl solutions were adjusted using 5M HCl and $NaNO_3$ solutions were adjusted with 5M HNO_3. Once 5-10 several acceptable cycles were recorded, the solutions were adjusted to pH 11.0 using 5M NaOH for NaCl and $NaNO_3$ solutions and 5M KOH for KCl solutions. A 12 N NaOH solution was used to ensure the solutions were not contaminated with carbonate. Changes in ionic strength resulting from pH adjustments were determined to be less than ≤1%. It is noteworthy to note that for each pH change, the sample surface was flushed at the new pH for a couple of days to ensure the surface was at the new pH before beginning the collection of exchange cycles. The pH of the influent and effluent solutions were monitored daily to ensure they remained consistent ± 0.2. The PZNC was determined by

plotting the heats of exchange (mJ/mg) verus solution pH. The pH at which the heats were equal was taken to indicate the PZNC, i.e., the pH where the net negative charge equals the net positive charge (Moghimi et al., 2013; Marcano-Martinez, 1989).

Additional Experiments on Rutile

The analysis of the rutile data revealed some observations that warranted additional investigations, as it will made clear in the next chapter. To further investigate these observations, additional experiments were performed on the rutile sample. The calorimetric heats of Na^+ and K^+ exchange were further measured under three additional experimental conditions. In addition to the solution pHs mentioned above, the heats of Na^+ and K^+ exchanges were also determined at pH of 2.0 using cycles of 50 mM NaCl and 50 mM KCl solutions.

To assess the potential impact of Cl^- on creating negative charge, a second experiment on rutile was performed, whereby the heats of Na^+ and K^+ exchanges were determined with NO_3^- as the background anion specie instead of Cl^-. Cycles of 50 mM $NaNO_3$ and 50 mM KNO_3 solutions were carried out under the same series of pH values used in the experiments ran in Cl^- (pH 2.0, 3.25, 5.8, and 11.0)

To explore the discrepancy between the heats of Na/**K** and K/**Na** exchange observed at high pHs on rutile, the heat of exchange of a third cation, Rb^+, was investigated. Cycles of 50 mM RbCl and 50 mM NaCl were performed to determine the heats of Na and Rb exchanges, while cycles of 50mM RbCl and 50mM KCl were used to measure the heats of K and Rb exchanges. The experiment was performed with unbuffered solution with an approximate pH of 5.8 and then again at pH 11.0. KCl and NaCl were adjusted to pH 11.0 as mentioned above and the RbCl solution was adjusted using 5M RbOH.

2.5 Ion Adsorption Density

The quantities of ion adsorbed, in μmol/mg, for each leg of the exchange cycles, were determined in a method designed to mimic the experimental conditions and complement the heat data from the flow experiments. Outside the calorimeter, approximately 40 mg of sample was packed into a glass column cell (identical to those used inside the calorimeter) of known weight. A programmable syringe pump was used to flush the samples surface with 50mM NaCl to saturate the exchange sites with Na^+ and Cl^- at same flow rates as the ones used to collect the heat data. The column was then removed, dried, and reweighed to determine the amount of excess NaCl that was entrained in the TiO_2 sample. Then, 50 mM $NaNO_3$ solution was pumped through the column and the effluent collected in a vial of known weight. The column was again removed, dried, and reweighed to determine the amount of entrained $NaNO_3$ solution. Similarly, cation adsorption density measurements were obtained by performing the above procedure with 50 mM NaCl and 50 mm KCl on the same sample. The concentration of NO_3^-, Cl^-, K^+, and Na^+ in the effluent was measured by High Pressure Liquid chromatography. The amount of anion or cations absorbed on the surface (μmol/mg) was calculated after correcting for the excess solution entrained in the sample. These ion adsorption densities were determined at pH 5.8, 3.25 and 11.0.

3 RESULTS AND DISCUSSION

3.1 Heats of Ion Exchange and Surface Charge

Anatase

Figure 3.8 presents representative raw data (calorimetric signal versus time) for C/**N** and N/**C**.[3.1.1] The heat signals of the Cl^- endotherm and NO_3^- exotherm on anatase at pH 5.8 were similar in terms of reaction times, shape and peak area as expected for a reversible ion exchange reaction.

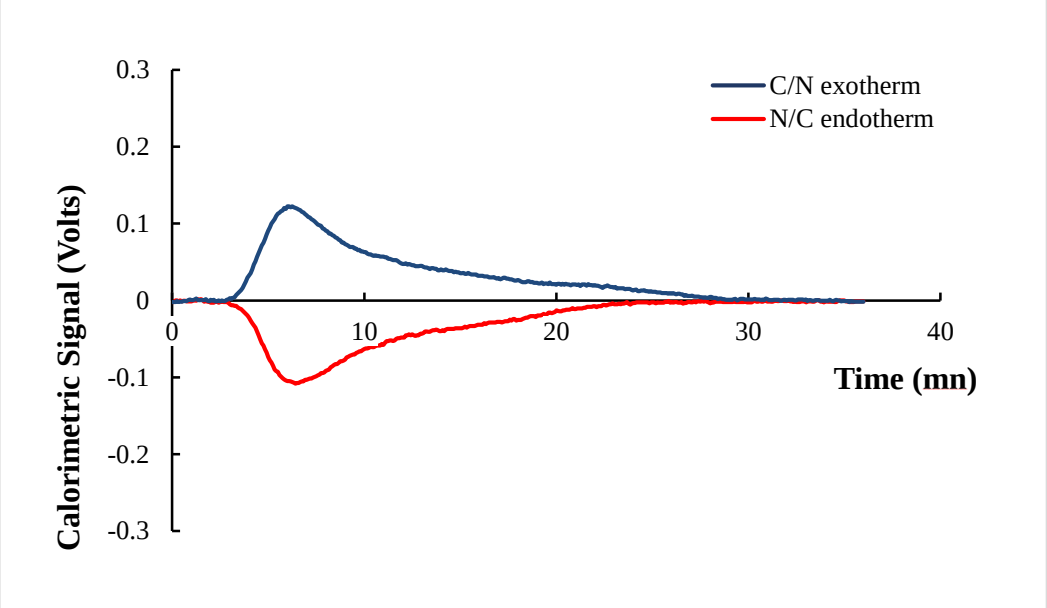

Figure 3.8. Heat Signals of Cl^- and NO_3^- Exchange at pH 5.8 on Anatase. (Y/**X** represents the exchange of ion Y by ion **X**).

The energy of the calorimetric heats of C/**N** and N/**C** exchange, Q_{exch} (mJ/mg), were converted to ΔH_{exch} (kJ/mol) using the measured sorption density, Γx (µmolx/mg), of the incoming ion in the exchange reaction (**X**). Table 3.4 lists these values determined from probing the positive and negative surface charge of anatase at pH 5.8.

Table 3.4. Heats of Ion Exchange and Surface Charge Values for Anatase at pH 5.8.

Surface Charge	Probe	Q_{exch} [b] (mJ/mg)	Γx (µmolx/mg)[c]	$\pm \Delta H_{exch}$ (kJ/mol)[e]

Positive (+)	N/**C**[a]	0.14 (0.01)[d]	0.040 (0.002)	3.5 (0.2)
	C/**N**	0.16 (0.01)	0.042 (0.009)	3.9 (0.8)
Negative (-)	K/**Na**	0.28 (0.02)	0.082 (0.008)	3.5 (0.3)
	Na/**K**	0.32 (0.01)	0.096 (0.005)	3.4 (0.2)

[a] Y/**X**, The exchange of ion Y by ion **X** used to probe the ± surface charge.
[b] Q_{exch}, Calorimetric heat of ion exchange probe Y/**X**.
[c] Γ_X, Sorption density (μmol_X /mg), amount (µmol) of probing ion (**X**) adsorbed on the surface (mg^{-1}) during the exchange.
[d] Numbers in parenthesis corresponds to ± one standard deviation.
[e] $\pm \Delta H_{exch}$, Molar enthalpy of ion exchange probe.

At pH 5.8, N/**C** exchange produced an endotherm with an average energy (Q_{exch}) of 0.14 $\pm$ 0.01 mJ/mg. The reverse exchange, C/**N**, was exothermic with Q_{exch} of - 0.16 $\pm$ 0.01 mJ/mg, essentially the same as the C/**N**. Using an average adsorption density of 0.041 $\pm$0.005 $\mu mol_{C(N)}$/mg (because of the equivalence of Q and Γ), the ΔH_{exch} for N/**C** and C/**N** on anatase was found to be equal to 3.7 $\pm$ 0.5 kJ/mol., with an understanding that although reported without a sign, the ΔH_{exch} will be negative for the exothermic leg (C/**N**) and positive for the endothermic portion (N/**C**) of the exchange cycle. While, to my knowledge, there are no other reported values of heats of chloride and nitrate exchange on anatase, this value falls in the range measured by Kabengi and Rhue (2006) who reported heats of Cl^- and NO_3^- exchanges ranging from 3.0 - 7.3 kJ/mol_c for amorphous aluminum hydroxide and by Gale et al. (2015) who reported a similar heat of 3.2 $\pm$ 0.5 kJ/mol_c on boehmite.

The cation exchanges (CE) exhibited similar characteristics to anion exchanges (AE), whereby the endotherm and exotherm were comparable in reaction times, shape and peak area (figure 3.9).

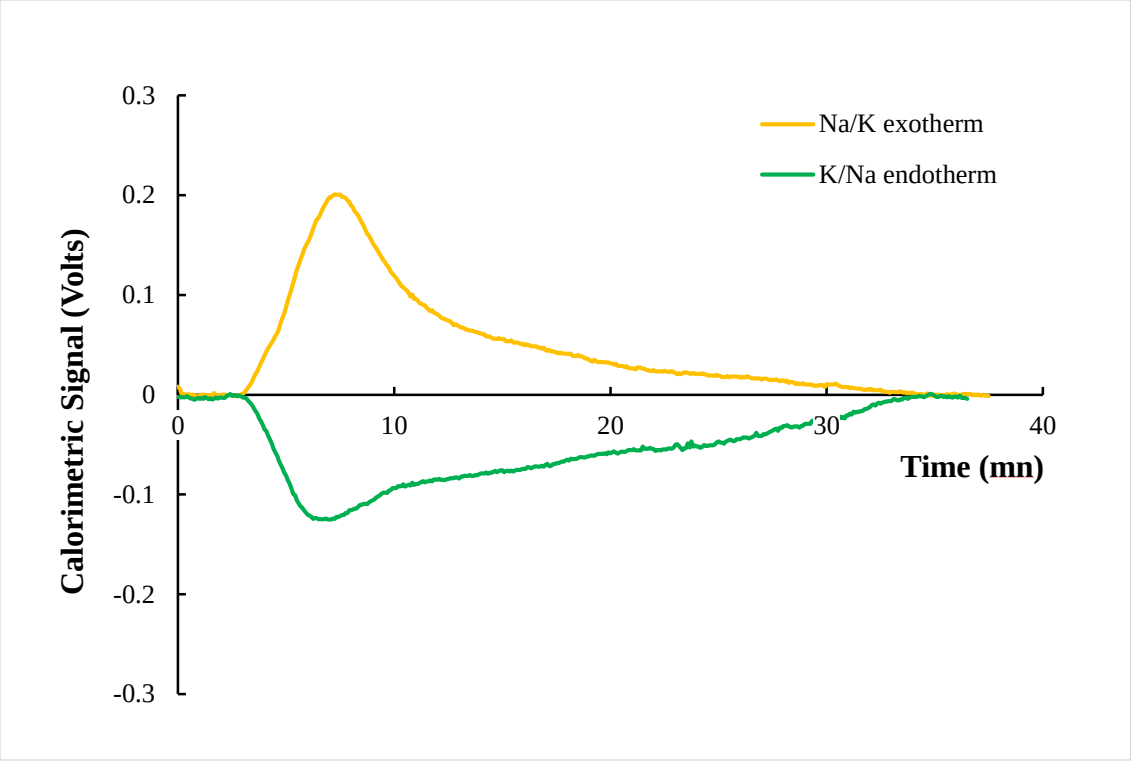

Figure 3.9. Representative heats Signals of K^+ and Na^+ Exchange at pH 5.8 on Anatase.

The exothermic exchange, Na/**K,** generated nearly the same amount of energy (- 0.32 ± 0.01 mJ/mg) as the endothermic exchange, K/**Na,** (+ 0.28 ± 0.02 mJ/mg). The Q (mJ/mg) values are slightly larger but comparable to the heat of Na^+ and K^+ exchange (0.15 ± 0.01 mJ/mg) measured by Gale (2013) using FAMC on a TiO_2 (P25) sample. This discrepancy can be explained by variation in sample composition whereby the P25 sample was found to be composed of ~ 86% anatase and ~14% rutile and hence with a significantly smaller SSA (~50 m^2/g) than the pure anatase sample used in this experiment. The Γ_{Na} and Γ_K were similar with an average of 0.089 ± 0.010 $\mu mol_{Na(K)}/mg$ resulting in a ΔH exchange value of 3.4 ± 0.2 kJ/mol. At pH 5.8, both heats of CE and AE were detectable indicating that anatase bore positive as well as negative charge. However, the Q_{CE} (mJ/mg) and the measured cation adsorption densities, Γ_C^+, were approximately two times larger in magnitude than that of the Q_{AE} and anion adsorption densities, Γ_A^-.

While the published literature on the ΔH_{exch} for both cations and anions exchange and adsorption remains somehow limited, the values obtained in this study are consistent to previous values obtained on MOs with FAMC and generally similar to other exchanges obtained through other methods and on other materials. For example, Gast (1972) reported calorimetric heats of exchange for alkali metal cations on Chambers montmorillonite ranging from a high of 10.4 kJ/mol for Li/Cs exchange, to a low of 0.4 kJ/mol for Li/Na exchange. Other researchers (Appel et al., 2003; Goudling and Talibudeen, 1984; Sparks and Jardine, 1981) have reported a ΔH for the K/Ca exchange on a variety of soils ranging from 3.3 to 16.3 kJ/mol$_c$. More pertinently, using titration calorimetry Machesky et al. (1991) measured the adsorption enthalpies of fluoride, iodate and phosphate onto goethite at pH 4.0 and found them to range from -25 kJ/mol to + 5 kJ/mol depending on surface coverage. While these are somewhat similar to the ranges obtained here, it is important to note that the anions reported in Machesky et al (1991) are expected to interact more strongly with MO surfaces and hence the enthalpies reported are for specific adsorption not exchange. Similarly higher values are also obtained when FAMC is used to measure adsorption enthalpies (Saburet al., 2015; Kabengi et al., 2006).

3.1.2

Rutile

Table 3.5 lists Q_{exch}, Γx, and ΔH_{exch} determined for rutile at pH 5.8. Figure 3.10 displays representative heat signals of Cl^- and NO_3^- exchanges.

Table 3.5. Heat of Exchange and Surface Charge Values at pH 5.8 on Rutile.

Surface Charge	Probe	Q_{exch} [b] (mJ/mg)	Γx ($\mu mol_x/mg$)[c]	$\pm \Delta H_{exch}$ (kJ/mol)[e]

Positive (+)	N/**C**[a] C/**N**	0.042 (0.003)[d] 0.056 (0.002)	0.015 (0.003) 0.014 (0.002)	2.9 (0.6) 2.5 (0.5)
Negative (-)	K/**Na** Na/**K**	0.042 (0.0004) 0.062 (0.001)	0.060 (0.011) 0.044 (0.012)	0.7 (0.1) 1.5 (0.2)

[a] Y/**X**, The exchange of ion Y by ion **X** used to probe the ± surface charge.
[b] Q_{exch}, Calorimetric heat of ion exchange probe Y/**X**.
[c] $\Gamma_{\mathbf{X}}$, Sorption density ($\mu mol_{\mathbf{X}}$ /mg), amount (µmol) of probing ion (**X**) adsorbed on the surface (mg^{-1}) during the exchange.
[d] Numbers in parenthesis corresponds to ± one standard deviation.
[e] $\pm \Delta H_{exch}$, Molar enthalpy of ion exchange probe.

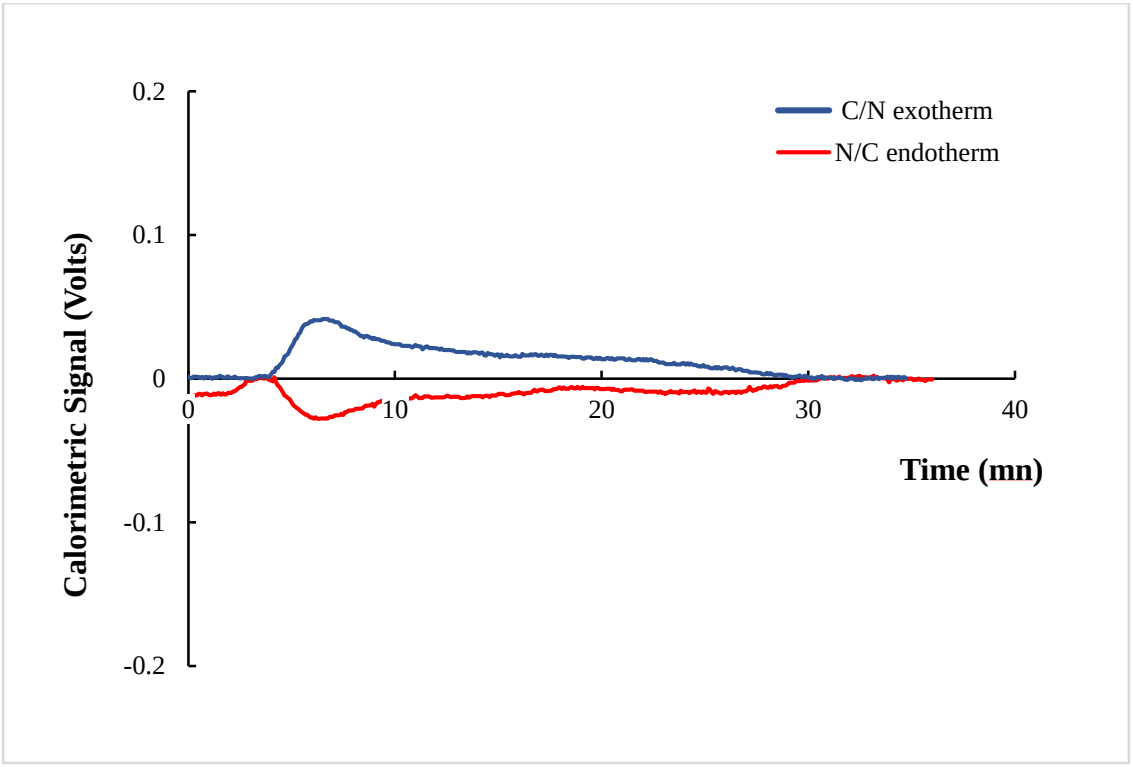

Figure 3.10. Heat Signals of Cl^- and NO_3^- Exchange at pH 5.8 on Rutile.

C/**N** exchange was found to be exothermic producing an average energy of - 0.056 ± 0.002 mJ/mg, and N/**C exchange** was endothermic with an average energy of +0.042 ± 0.003 mJ/mg. Using an adsorption density of 0.015 ±0.003 μmol_{NO3}/mg, the ΔH_{exch} of C/**N** was -2.9 ± 0.6 kJ/mol_c and using adsorption density of 0.014 ±0.002 μmol_{Cl}/mg, the ΔH_{exch} of N/**C** was +2.5 ± 0.5 kJ/mol_c.

Figure 3.11 shows representative heat signals of Na^+ and K^+ exchanges.

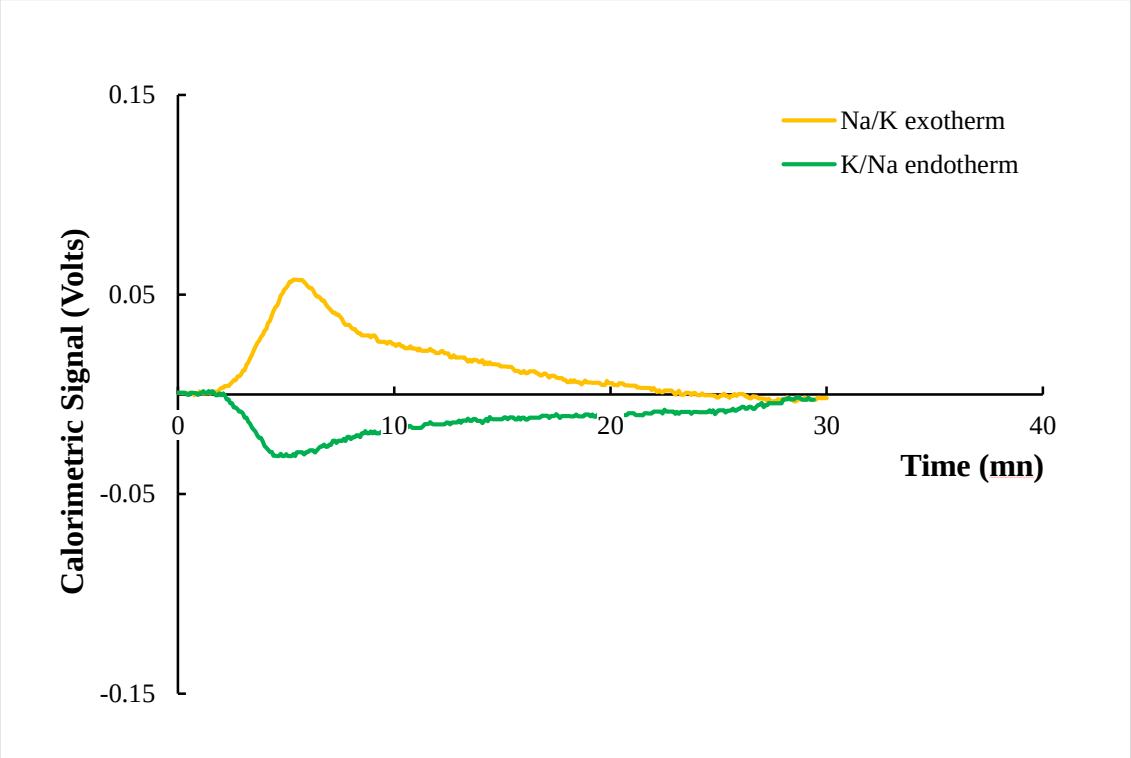

Figure 3.11. Heat Signals of Na+ and K+ Exchange at pH 5.8 on Rutile.

The exothermic Q_{exch} of Na/**K** was - 0.062 ± 0.001 mJ/mg, and the endothermic Q_{exch} of K/**Na** was + 0.042 ± 0.0004 mJ/mg. The Na/**K** exchange produced approximately 30% more energy than the reverse K/**Na** reaction. The significant difference in heats indicates that the endothermic reaction, K/**Na**, was considerably less energetic than the exothermic reaction, Na/**K**, at pH 5.8. The adsorption density measurements also showed a similar but inverse deviation, whereby more Na^+ (0.060 ±0.011 $\mu mol_{Na^+}/mg$) is shown to have absorbed on the rutile surface than K^+ (0.044 $\mu mol_{K^+}/mg$). Taking into account the respective Γ_{Na} and Γ_K, the ΔH_{exch} for K/**Na** was + 0.7 ± 0.1 kJ/mol and that for Na/**K** was -1.5 ± 0.2 KJ/mol. The larger ΔH_{exch} of Na/**K** suggests the displacement of Na^+ by K^+ is more energetic than the displacement of K^+ by Na^+ in the reverse K/**Na** reaction.

Similarly, to anatase, Q_{exch} and $\Gamma_{\mathbf{X}}$ for both cations and anions were detectable for rutile at pH 5.8 suggesting the surface bore both positive and negative charge. However, some notable differences between anatase and rutile were observed. On anatase, the Q_{exch} and $\Gamma_{\mathbf{X}}$ for cations were two times larger than those for anions. On rutile, however, the Q_{exch} of anions and Q_{exch} of cations were much more comparable, the $\Gamma_{\mathbf{C}^+}$ were significantly higher, almost by a factor of 5, compared to the $\Gamma_{\mathbf{A}^-}$. Furthermore, on rutile the heat of Na/**K** exchange was significantly higher than that of K/**Na** exchange, while there was no significant incongruence in Q_{exch} on anatase. The differences between rutile and anatase can be related to the proximity of the experimental 5.8 pH to the PZC of each surface, whereby the magnitude of either the positive or negative charge changes in a different manner according to which sites are protonating and deprotonating. However, these differences seem to additionally reflect some inherent mechanistic differences in the way cations and anions interact with the surface of each polymorph as it will be discussed later (for example, the inner sphere complexation of Cl^- with rutile surface TOs).

Another difference between anatase and rutile is the magnitude of the incongruence between Na^+ and K^+ heats of exchange and charge densities, with rutile exhibiting significantly more heats and smaller adsorption densities associated with Na/**K** than K/**Na** (by a factor of ca. 1.5) than anatase for which the Na/**K** heats and adsorption densities are only 1.14 times bigger and smaller respectively than those of K/**Na**. The larger incongruence between K and Na on rutile suggests that the probing cation has a stronger impact on its charge development than that of anatase. This behavior may be related back to the discussion on the role of the mineral dielectric constants in section 1.2. Specifically rutile having a higher dielectric constant (114) will have significantly different equilibrium constants, following the order: $Li^+ > Na^+ > K^+ > Rb^+$ and Cs^+. Anatase on the other hand, is characterized as a surface with an intermediate dielectric constant and is not

predicted to have different equilibrium constant for different cations (Sverjensky, 2005). This discrepancy between anatase and rutile charging will be further explored as the same measurements were made at other pHs as described in the section below.

3.2 Charging Curves and Point of Zero Net Charge

Kabengi et al (2006) demonstrated that calorimetric heats of anion (AE) and cation exchange (CE) are directly proportional to the positive and negative surface charge, respectively, and that measuring heats of cation and anion exchanges at different pHs is a calorimetric method to determine the zero point of net charge.

3.2.1 *Anatase*

Table 3.6 lists the heats of exchange and adsorption density values determined at pHs 3.25, 5.8, and 11.0 for anatase.

Table 3.6. Heats of Exchange and Surface Charge Values at Various pHs for Anatase

pH	Surface Charge	Probe	Q_{exch} [b] (mJ/mg)	Γx (μmol$_X$/mg)[c]	± ΔH_{exch} (kJ/mol)[e]
3.25	Positive (+)	N/**C**[a]	0.49 (0.01)[d]	0.30 (0.01)	1.6 (0.03)
		C/**N**	0.50 (0.03)	0.25 (0.01)	2.0 (0.09)
	Negative (-)	K/**Na**	0.090 (0.003)	ND[d]	NA[e]
		Na/**K**	0.13 (0.00)	0.037 (0.005)	3.4 (0.5)
5.8	Positive (+)	N/**C**	0.14 (0.01)	0.040 (0.002)	3.5 (0.2)
		C/**N**	0.16 (0.01)	0.042 (0.009)	3.9 (0.8)
	Negative (-)	K/**Na**	0.28 (0.02)	0.080 (0.1)	3.5 (0.3)
		Na/**K**	0.32 (0.01)	0.096 (0.005)	3.4 (0.2)
11	Positive (+)	N/**C**	0.046 (0.003)	0.020 (0.002)	2.4 (0.3)
		C/**N**	0.028 (0.004)	0.023 (0.003)	1.3 (0.1)
	Negative (-)	K/**Na**	2.20 (0.03)	0.69 (0.01)	3.2 (0.1)
		Na/**K**	2.50 (0.05)	0.69 (0.01)	3.6 (0.0)

[a] Y/**X**, The exchange of ion Y by ion **X** used to probe the ± surface charge.
[b] Q_{exch}, Calorimetric heat of ion exchange probe Y/**X**.
[c] Γx, Sorption density (μmol$_X$ /mg), amount (μmol) of probing ion (**X**) adsorbed on the surface (mg^{-1}) during the exchange.
[d] Numbers in parenthesis corresponds to ± one standard deviation.
[e] ± ΔH_{exch}, Molar enthalpy of ion exchange probe.

Figure 3.12 displays representative calorimetric signals for C/**N** and N/**C** exchanges. As pH decreased from 5.8 to 3.25, the heat signals increased in peak area, indicating an increase in the surface positive charge. While as pH increased from 5.8 to 11.0, the calorimetric peaks decreased indicating a decrease in the surface positive charge. The persistence of small peaks for C/N and N/C exchanges demonstrate that the surface still bore some positive charge at the high pH of 11.0.

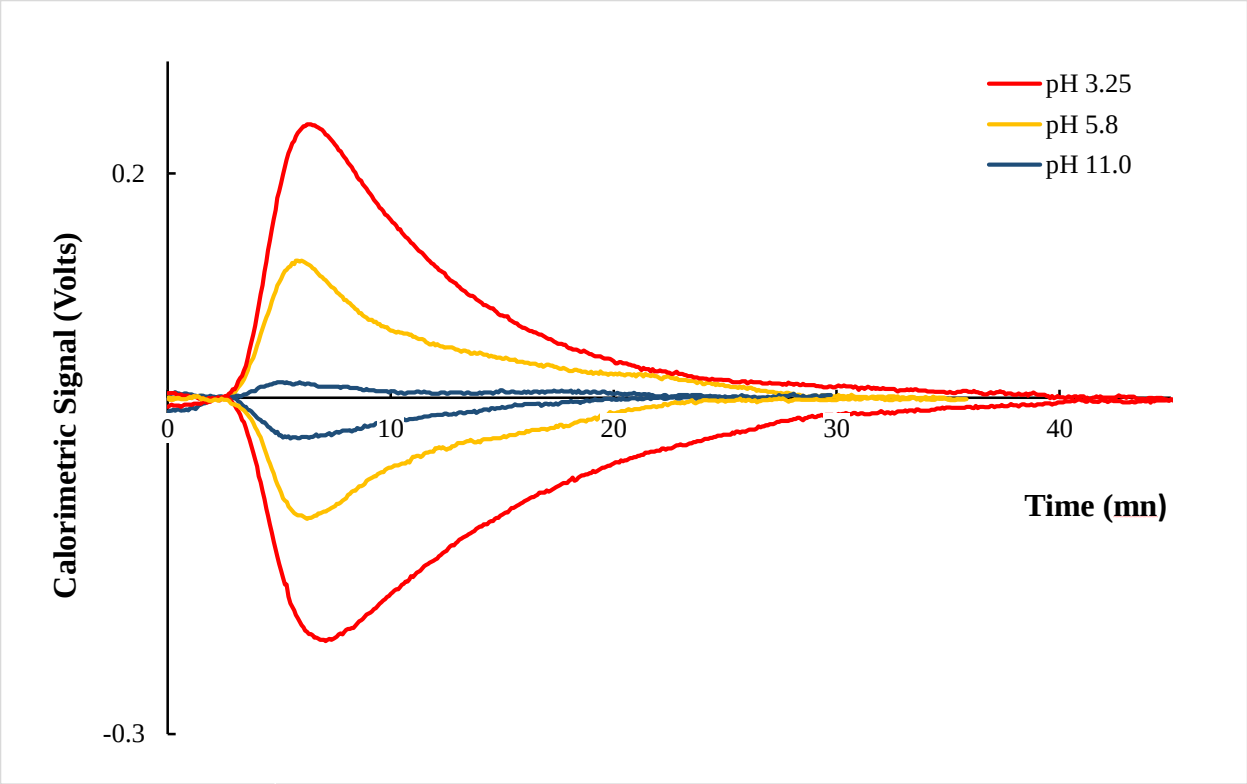

Figure 3.12. Heats signals of C/N (exotherms) and N/C (endotherms) exchange at various pHs on Anatase.

Figure 3.13 shows the heat signals for Na/**K** and K/**Na** exchanges obtained at the three pH values. Heats of cation exchange showed the opposite trend to those of anion exchange. As pH increased, the peaks increased in size, indicating an increase in negative surface charge, while as pH decreased to 3.25 the peaks also decreased to reflect a decrease in the surface negative charge. In this case as well, the presence of small cation exchange peaks shows that the surface still bore some negative charge at pH 3.25. This behavior may be understood using the site density map obtained by Bourikas et al (2001) shown in figure 1.6. Although, it was generated for a P25 titania sample composed of only 80% w/w anatase in 0.1 M solution and is not an exact representation of the anatase and conditions of this experiment, they are reasonably close as to assume some similarities. Thus, the presence of negative charge at pH 3.25 arises from the non-protonated TO (i.e. $TiO^{-0.35}$) and positive charge at pH 11.0 on anatase from the protonated BO ($Ti_2OH^{+0.43}$).

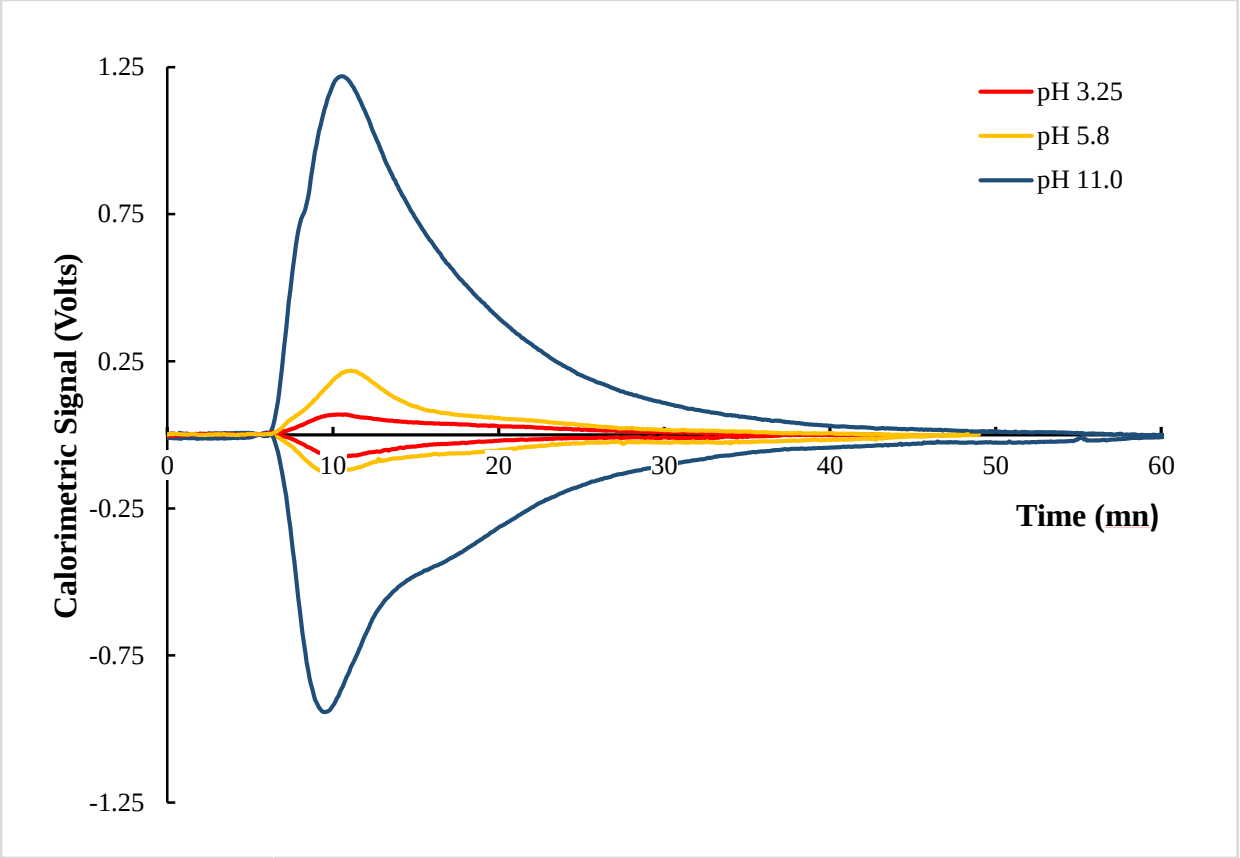

Figure 3.13. Heats signals of K^+ and Na^+ exchange at various pHs on Anatase.

The PZNC was determined from a plot of the heats of exchange (mJ/mg) versus pH (Figure 3.14). The PZNC, taken as the pH at where the heats of cation exchange (CE) and anion exchange (AE) were equal, was found to be 5.3.

Kosmulski (2002) gathered over 30 published PZC values for anatase. Those ranged from 4.8 to 6.5 with a calculated a median of 5.5 and an average of 5.9. However, the anatase used in most of the studies referenced in his paper had a significantly smaller specific surface area than the nanocrystalline sample used in this experiment. A study published by Ridley et al. (2013), who performed potentiometric titrations in NaCl media at similar ionic strength on the same ST-01 anatase sample used in this experiment, found the pH of zero net proton charge (pHznpc) to be 6.42 ± 0.02. Due to the inherent difference in the nature of what is being measured, it does not

seem accurate to assume equality between the PZNC measured here and the PZNPC charge reported in the aforementioned paper.

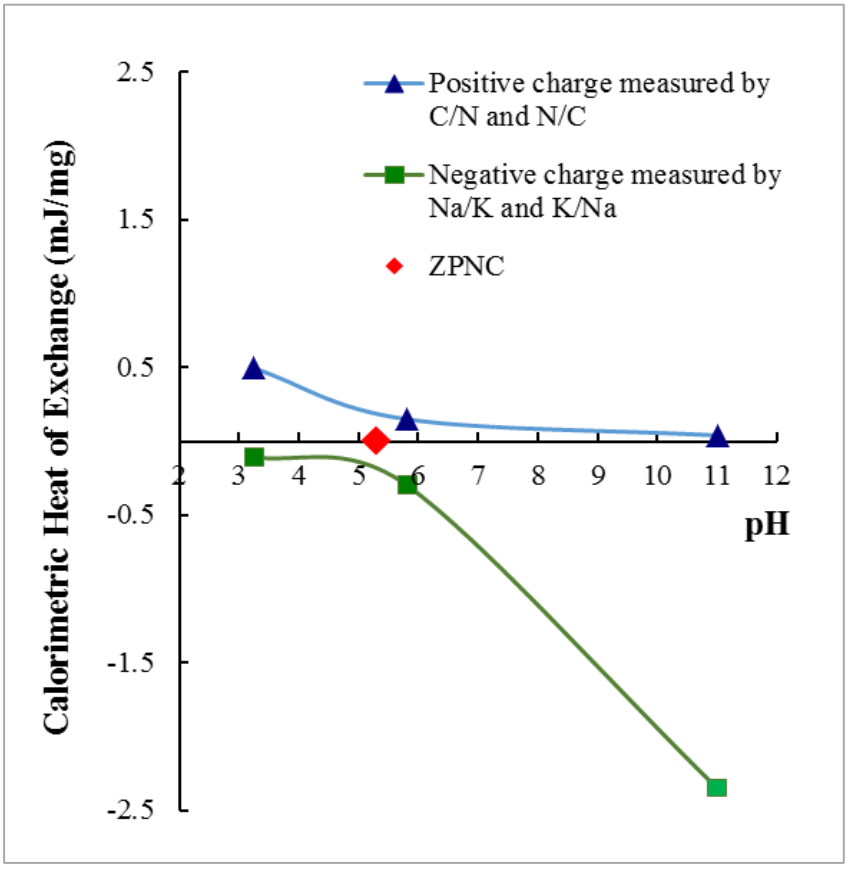

Figure 3.14. Anatase charging curve. Heats of anion exchange and cation exchange (mJ/mg) plotted against solution pH. The diamond indicates the PZNC (~pH 5.3).

3.2.2

Rutile

Table 3.7 lists the heats of exchange and charge density values determined at pH values 3.25, 5.8, and 11.0 on rutile. Due to the relatively small amount of anions adsorbed at pH 11.0 and cations at pH 3.25, some values could not be quantified analytically and are presented in the table as ND for non-detectable. This highlights the increased sensitivity FAMC offers in probing surface charge as compared to other macroscopic methods. In fact, as will become clearer in the future

section when titration data are evidenced, FAMC is capable of separating surface charge in various cations with a significantly better resolution. Figure 3.15 displays representative calorimetric signals of Cl^- and NO_3^- exchanges at each pH on rutile. As expected, increasing pH resulted in decreased Cl^- and NO_3^- peaks areas indicating a decrease in the positive surface charge. At pH 11.0, the presence of small peaks for Cl^- and NO_3^- exchanges demonstrated that the surface still bore some positive charge, albeit being below the detection limit of a quantitative determination by HPLC-IC.

Table 3.7. Heats of Exchange and Surface Charge Values at Various pHs on Rutile

pH	Surface Charge	Probe	Q_{exch} [b] (mJ/mg)	Γx (μmolx/mg)[c]	± ΔH_{exch} (kJ/mol)[e]
3.25	Positive (+)	N/**C**[a]	0.066 (0.002)[d]	0.040 (0.0010)	1.4 (0.3)
		C/**N**	0.068 (0.001)	0.030 (0.010)	2.2 (0.7)
	Negative (-)	K/**Na**	0.020 (0.001)	ND[f]	NA[g]
		Na/**K**	0.040 (0.002)	0.041 (0.004)	1.0 (0.1)
5.8	Positive (+)	N/**C**	0.042 (0.003)	0.015 (0.003)	2.9 (0.6)
		C/**N**	0.056 (0.002)	0.014 (0.002)	4.2 (0.5)
	Negative (-)	K/**Na**	0.042 (0.0004)	0.060 (0.011)	0.7 (0.1)
		Na/**K**	-0.062 (0.001)	0.044 (0.012)	1.5 (0.2)
11	Positive (+)	N/**C**	0.022 (0.001)	ND	NA
		C/**N**	0.022 (0.001)		
	Negative (-)	K/**Na**	0.262 (0.011)	0.101 (0.007)	2.6 (0.2)
		Na/**K**	0.340 (0.005)	0.085 (0.006)	4.0 (0.3)

[a] Y/**X**, The exchange of ion Y by ion **X** used to probe the ± surface charge.
[b] Q_{exch}, Calorimetric heat of ion exchange probe Y/**X**.
[c] Γx, Sorption density (μmolx /mg), amount (μmol) of probing ion (**X**) adsorbed on the surface (mg^{-1}) during the exchange.
[d] Numbers in parenthesis corresponds to ± one standard deviation.
[e] ± ΔH_{exch}, Molar enthalpy of ion exchange probe.
[f] ND, Not detected.
[g] NA, Not available.

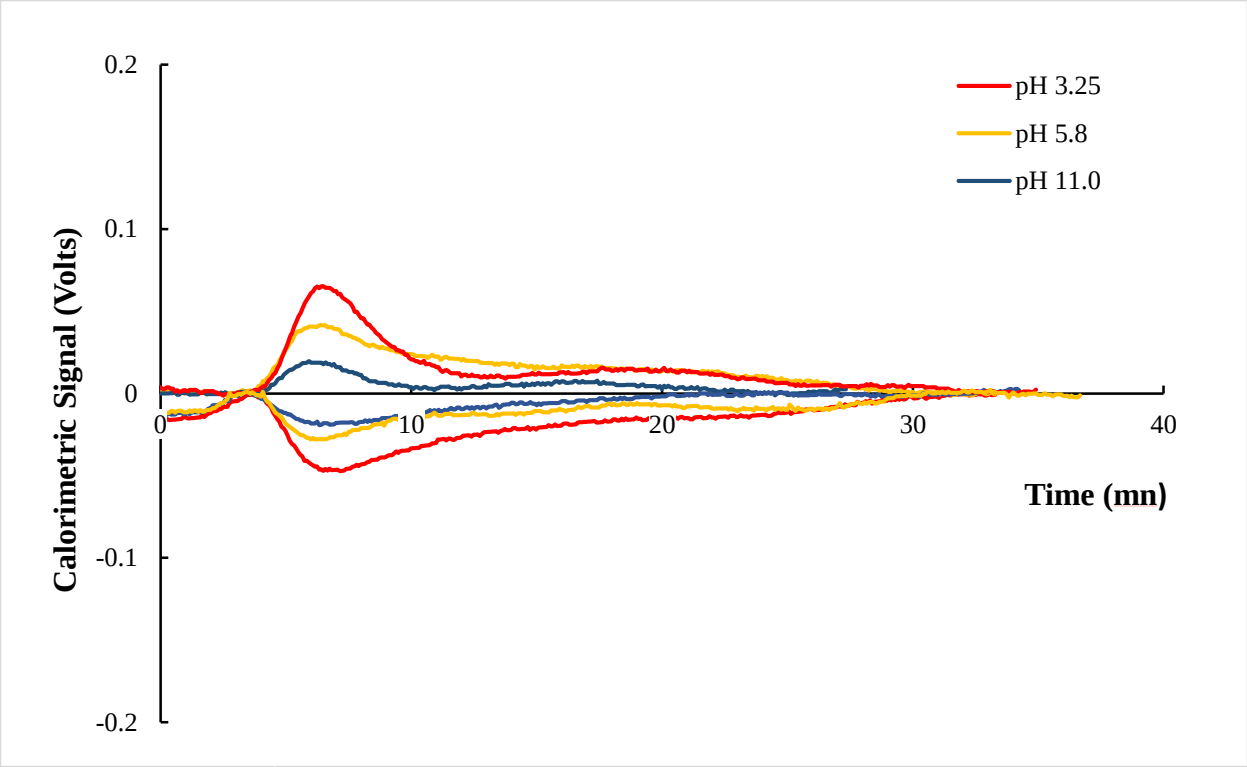

Figure 3.15. Heat Signals of Cl^- and NO_3 Exchange at Various pHs on Rutile.

Figure 3.16 shows representative heat signals for K^+ and Na^+ exchange obtained at the three pH values. Heats of cation exchange showed the opposite trend of anion exchange. As pH increased, the K^+ and Na^+ peaks increased in size, indicating an increase in negative surface charge. At pH 3.25, the presence of K^+ and Na^+ exchange peaks shows that the surface still bore some negative charge, again although being unquantifiable using an HPLC-IC. It is noteworthy to mention the incongruence that exists between K/**Na** and Na/**K** whereby the heats associated with the latter exchange are significantly and consistently bigger than those of the former, and the sorption density values consistently and significantly lower.

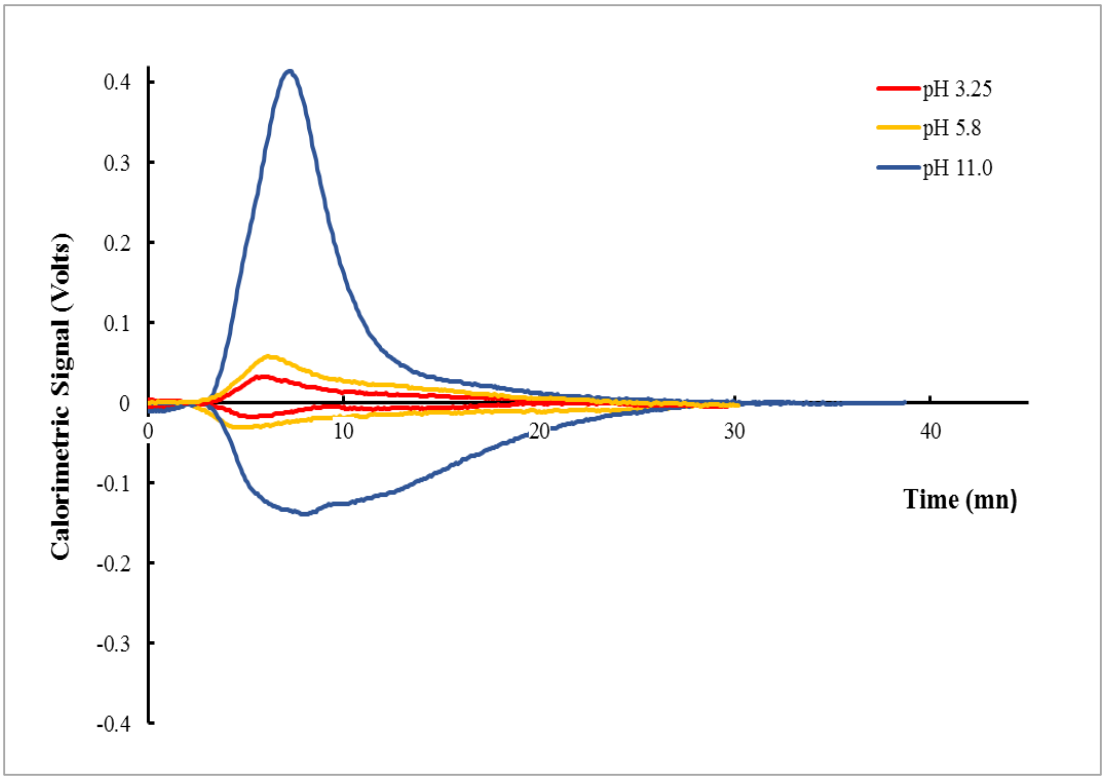

Figure 3.16. Heat Signals of K+ and Na+ Exchange at Various pHs on Rutile.

Figure 3.17 displays the charging curve for rutile. As discussed above, the heat of K/**Na** exchange was significantly smaller than the heat produced by Na/**K**. Consequently, the pH at which the PZNC occurred depending on which cation exchange reaction was used to probe the negative surface charge. When the heat of exchange of Na/**K** was used, the PZNC was found to be 5.4 which is the same value often reported for rutile in the literature (Machesky et al., 1994; Kosmulski, 2002). When the negative surface charge was probed using the heat of K/**Na** exchange, the PZNC was determined to equal 5.8. This difference in the PZNC determination highlights the impact the probing cation can have on the surface charge of rutile and the need for careful examination of the experimental protocol when comparing values from different sources. It should also be mentioned that although the heat of N/**C** was significantly different than that of C/**N** at pH 5.8, their magnitudes at the other pHs were in closer agreement with each other and the overall

change in magnitude at pH 5.8 was not significant enough to affect the PZNC determination. However, the observation serves to highlight the greater impact the negative surface species imparts on the charging behavior of rutile over a wide range of pH values compared to the positive surface charge species.

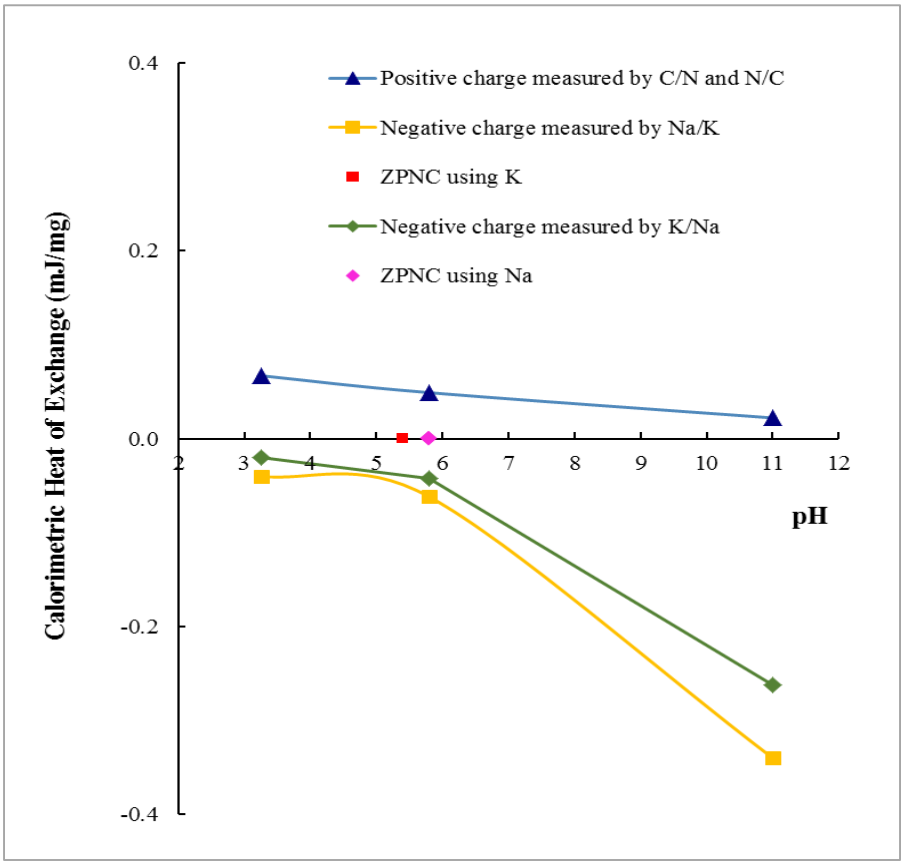

Figure 3.17. Rutile charging curve. Heats of anion exchange and cation exchange (mJ/mg) of rutile versus solution pH. The diamond indicates the PZNC when measured with Na^+ (~pH 5.8) and the purple square indicates the PZNC when measured using K^+ (~pH 5.4).

3.3 Incongruence of K^+ and Na^+ Exchange on Rutile

On rutile, the heat of K/Na was lower than the heat of Na/K by 50%, 33% and 23% at pHs 3.25, 5.8 and 11.0 respectively. Since the heats of K/Na and Na/K exchange at all pH conditions were consistently unequal in magnitude, it seemed fair to assume that the magnitude of the surface negative charge was equally incongruent in Na and K and is hence depending on which cation is

present on the surface. The measurements of the ion sorption densities revealed that more Na^+ was adsorbed on the surface than K^+ at both pH 5.8 and 11.0 by 26% and 19 % respectively. At pH 3.25 the sorption density measurements were not attainable analytically as they were below the HPLC-IC detection limit, underscoring again the fact that calorimetric heats are significantly more sensitive to charge and surface processes.

Differences in rutile charging behavior in the presence of various cations sorption have been noted by Machesky et al. (2015) who reported charging data in a study on CD-MUSIC surface complexation model parameters (constrained using classical molecular dynamic (CMD) simulations) to describe rutile titrations in RbCl and NaCl media under a range of temperatures. Their results, presented in Figure 3.18, showed that the rutile surface possesses more negative charge in the presence of Na^+ than in Rb^+. The difference between the surface charge in Na^+ and that in Rb^+ becomes increasingly bigger and clearer at increasingly alkaline pH values. At pHs lower than 6, it seems the macroscopic titrations did not detect a difference in the surface charge in either cation. Similarly, the ion sorption densities values in this study were not resolved at pH 3.25 due to analytical obstacles. Yet the significant differences in the calorimetric heats of Na/K and K/Na at pH 3.25 seems to suggest the surface charge to be different in K^+ than in Na^+ even at this low pH.

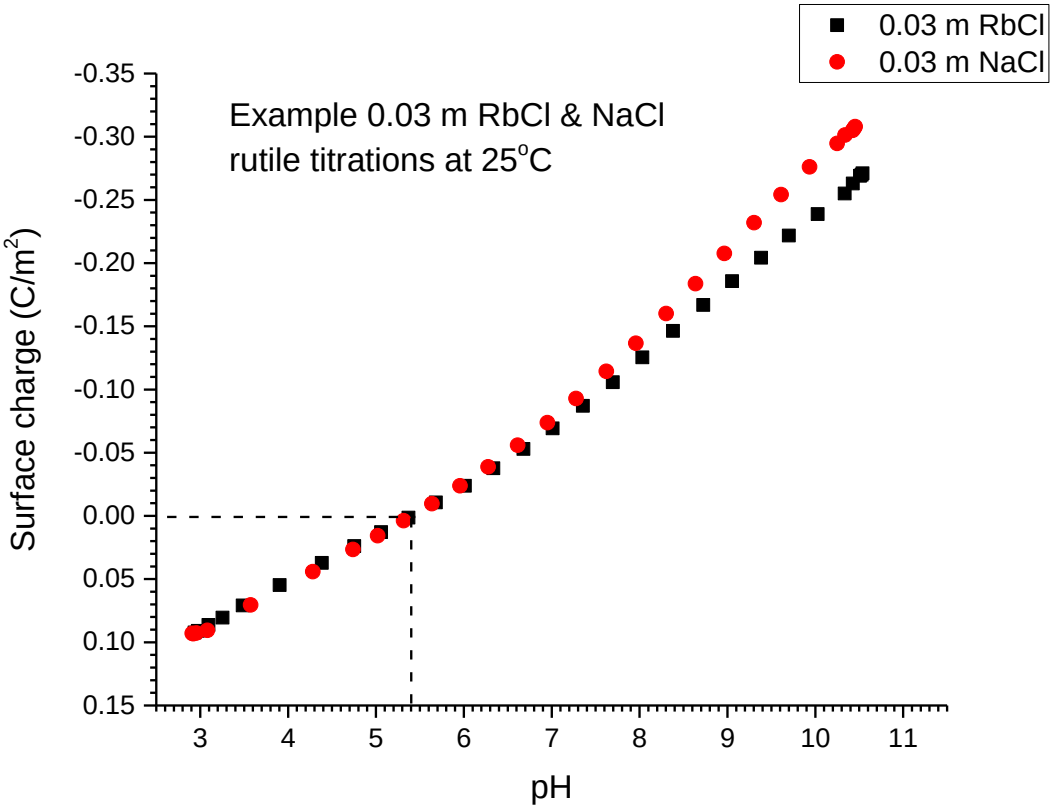

Figure 3.18. Titration data on Rutile (Machesky et al, 2015).

While the results from Machesky et al. (2015) contrast Na^+ and Rb^+, it is expected that K^+ interacts with the rutile surface in a similar fashion as Rb^+. In fact, the hydration radius and hydration enthalpy of K^+ (3.31 Å, -322 kJ/mol) are more similar to those of Rb^+ (3.29 Å, -293 kJ/mol) than either are to Na^+ (3.58Å, -409 kJ/mol). Hence, the heat of Rb^+ and K^+ exchanges would be closer in magnitude than that of either Na^+ with K^+ and Na^+ with Rb^+.

To test the validity of this assumption, the heats of Rb^+ and Na^+ and Rb^+ and K^+ exchanges were measured at pH 5.8 and 11.0. Table 3.8 lists the results of these measurements and figure 3.19 displays the representative raw calorimetric heat signals

Table 3.8. Heats of Rb^+ Exchange with K^+ and Na^+ at pH 5.8 and 11.0.

pH	Probe	Q_{exch} (mJ/mg)	$\frac{X/\mathbf{Y}^c}{Y/\mathbf{X}}$	$\frac{K/\mathbf{Na}^d}{Na/\mathbf{K}}$
5.8	Rb/**Na**[a]	0.071 (0.005)[b]	0.67	0.68
	Na/**Rb**	0.106 (0.009)		
	Rb/**K**	0.035 (0.003)	0.90	
	K/**Rb**	0.039 (0.002)		
11	Rb/**Na**	0.144 (0.001)	0.57	0.77
	Na/**Rb**	0.251 (0.008)		
	Rb/**K**	NA	NA	
	K/**Rb**			

[a] Y/**X**, the exchange of ion Y by ion **X**.
[b] Numbers in parenthesis corresponds to ± one standard deviation.
[c] Ratio of less energetic exchange to more energetic exchange.
[d] Ratio of K^+ and Na^+ Q_{exch} from Table 3.7.

The calorimetric heats of exchange of Rb^+ and Na^+ were found to match perfectly the incongruence previously measured between K^+ and Na^+. The energy of Rb/**Na** exchange was 33% and 26% lower than that of Na/**Rb** at pHs 5.8 and 11.0 respectively. These results confirm that indeed Rb^+ interacts with the rutile surface similarly to K^+. Furthermore, energies of the Rb/K and K/Rb exchanges were found to be essentially the same.

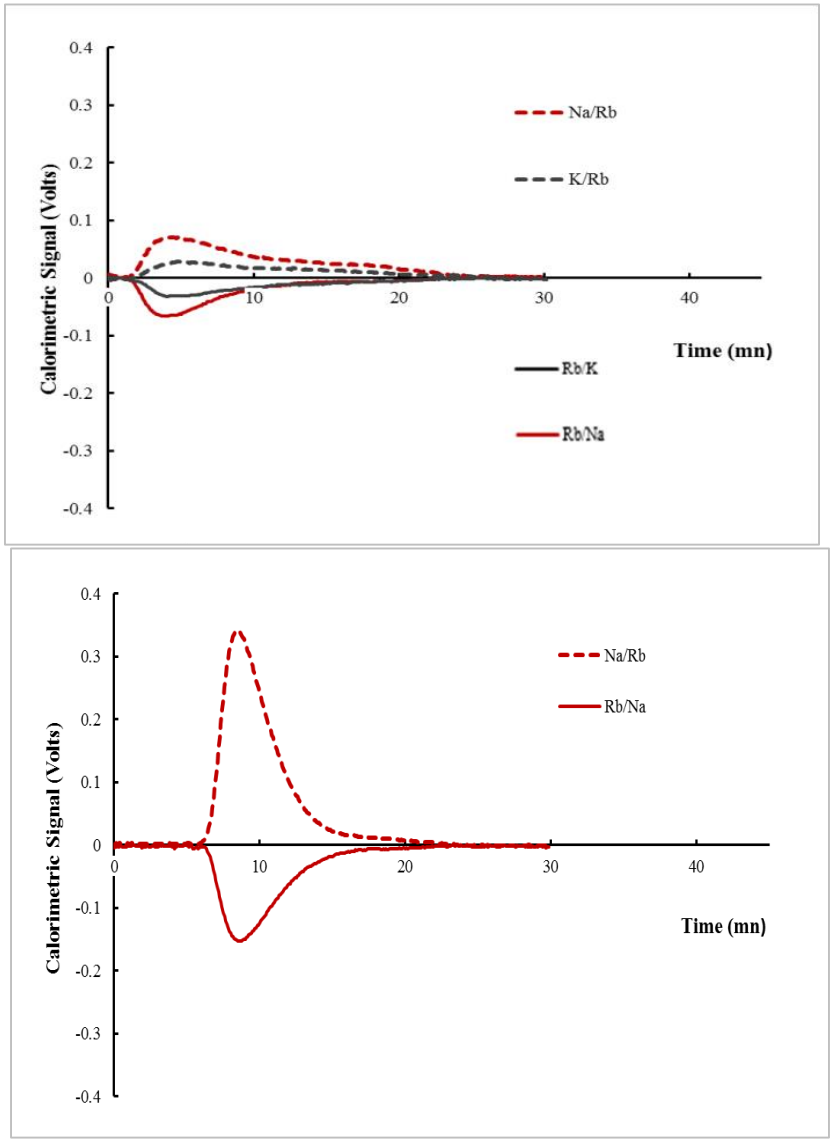

Figure 3.19. Calorimetric heat signals of Rb+ exchanges with Na+ and K+ at pH 5.8 (top) and Rb+ exchanges with Na+ at pH 11.0 (bottom).

The heat of exchange is the summation of many reactions: dehydration and adsorption of incoming species along with desorption and rehydration of the exchanged species (Ferreier et al., 2013). Thus, the source of the incongruent behavior of ions on rutile must extend from one of these processes. It might be assumed that during the Na/**K** exchange the larger amount of Na^+ rehydrating as it enters the solution exceeds the smaller amount of K^+ dehydrating to adsorb on

the surface. In other words, the exothermic rehydration of Na^+ leaving the surface consumes the endothermic dehydration of K^+ adsorbing onto the surface due to the larger amount of Na^+ species being displaced from the surface and the larger hydration enthalpy of Na^+. These factors result in a large greater exothermic reaction. However, in the reverse exchange, K/**Na**, the endothermic dehydration of more Na^+ species should consume an equal amount of the exothermic rehydration of K^+ entering solution as it did in the reverse reaction and thus results in an overall endothermic displacement of K^+ by Na^+. The incongruence between these two repeated cycles suggests that the cations are not adsorbing to the rutile surface in the same way (losing different hydration waters, different geometries, different bond lengths to the surface, different distances from the surface, etc.) resulting in differences in surface charge and thus the differences in calorimetric heats of exchange. Similar observations were seen by Ferreier et al. (2013) when using FAMC to measure the heats of Na^+ and Ca^{2+} exchange on zeolites. The data from one sample (zsm-5) displayed a significant dissimilarity between the endotherm and exotherm attributed to a difference in adsorption mechanisms whereby Na adsorbed as inner-sphere and Ca adsorbed as outer sphere (Ferreier et al., 2013). Although it has been shown that inner-sphere binding is favored by both Rb^+ and Na^+ at neutral and negative surface charge conditions on rutile, they do not necessarily bind in the same geometric configurations (Predota et al., 2013). The CMD simulations conducted by the same authors in a series of papers revealed that tetratdentate binding (TD) predominates as the inner most adsorption mode for the larger Rb^+ cation at neutral and negative charge conditions due to the relatively ease in removal of its hydrated water molecules (Machesky et al., 2015). For Na^+, bidentate geometry (BD) was shown to be favored at neutral charge conditions but moves towards TD binding with increasing negative surface charge as more hydrated water molecules are

able to be removed (Predota et al., 2013). Figure 3.20 shows the binding geometries of TD and BD sites (Wesolowski et al., 2008).

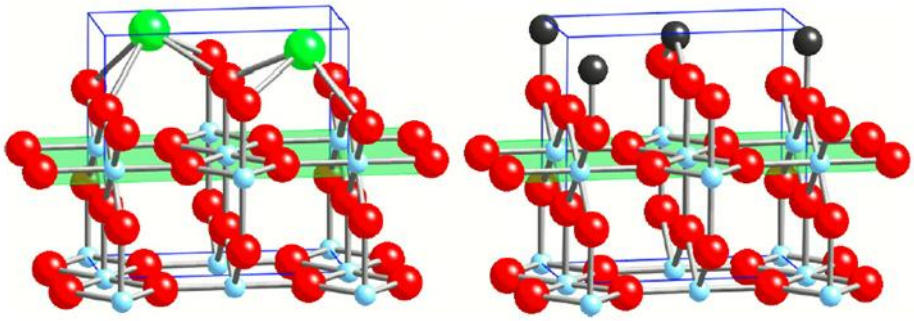

Figure 3.20. Dominate Binding Geometry of Rb^+ (left, tetradentate) and Na^+ (right, bidentate) at negative surface charge conditions (Wesolowski et al, 2008).

TD sites brings cations closest to the surface where the cation is bound to two underlying terminal oxygens (TO) and two bridging oxygens (BO). BD sites are farther from the surface. The BD site where the cation is bound with one BO and one TO (denoted BOTO) sits closer to the surface than the outermost BD site where a cation is bound with two TO (TOTO) (Predota et al., 2013). It has been shown that, cations sorb at sites progressively closer to the rutile surface with decreasing hydration energy for any given coordination mode, thus Rb^+ (and/or K^+) in TD configuration sits closer to the Ti surface than Na^+ in TD configuration (Predota et al., 2013).

At pH 5.8, where Rb^+ sits predominately in TD and Na^+ predominately BD, the displacement of Rb^+ by Na^+ results in the overall endothermic reaction of the exchange plus the endothermic partial-dehydration energy of (~2 water molecules on) Na^+ to allow its BD binding and the subsequent exothermic partial-rehydration of (~4 water molecules on) Rb^+ after its release from TD binding site. Since that heat of exchanges between Rb^+ and K^+ are closer in magnitude

than that of Na^+ and K^+ then the assumption that K^+ behaves similarly to Rb^+ seems reasonable. Thus it seems that the difference in the geometry, denticity, and strength of ion binding at neutral and high pH values causes the observed differences in heats of K/**Na** and Na/**K** (and Na/**Rb** and Rb/**Na**).

3.4 The Impact of Cl^- on the Negative Surface Charge Development of Rutile

It has been suggested in the literature that Cl^- has an effect on surface charge of rutile at low pHs. The CMD simulations ran by Machesky et al. (2015) observed Cl^- displacing some terminal water molecules at low pHs on rutile. The axial density profiles (figure 3.21) generated from their study reveals Na^+ not only sits closer to the rutile 110 surface than Rb^+ at positive surface charge, but also results in a larger concentration of Cl^- ions adsorbed in an inner-sphere arrangement from the displacement of water molecules at terminal Ti atoms, represented by the inner most peak at about 3.0 Å (Machesky et al., 2015). The decrease in terminal oxygens due to the adsorption of Cl^- would mean a decrease in the negatively charged TiO^- sites for Rb^+(K^+) to bind in its dominant tetradentate configuration and less TOTO bidentate sites available for Na^+ leaving the BOTO to become its dominant bidentate configuration at low pH.

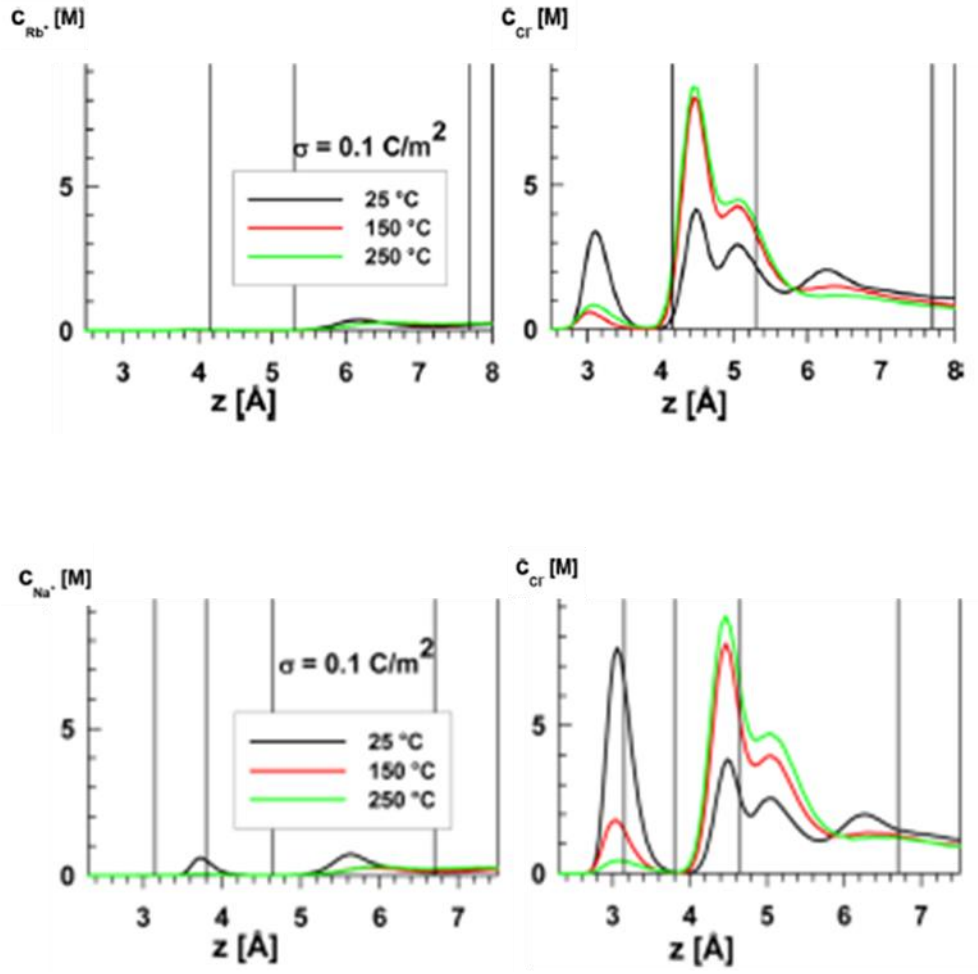

Figure 3.21. Axial density profiles of RbCl (top) and NaCl (bottom). Rb^+ (top left) and Cl^- (top right) for RbCl solutions and Na^+ (bottom left) and Cl^- (botom right) for NaCl solutions at the nonhdroxylated rutile (110) surface, as function of temperature and surface charge density. z (Å) denotes the distance above the Ti-O surface plane (Machesky et al., 2015).

The specific adsorption of Cl^- at positive surface charge could explain the discrepancy in the heats of Na/**K** and K/**Na** exchange seen on rutile and why the phenomenon is not observed on anatase. It could also be related to the fact that at pH 3.25 Na/**K** exchange generated a significant amount of heat (0.040 ± 0.02 mJ/mg) almost equal to that obtained for N/**C** and C/**N** exchanges at pH 5.8, even though pH 3.25 is 2-3 pH units below the PZC. In an earlier section, this negative charge was attributed to the non-protonated TO (i.e. $TiO^{-0.35}$) that start showing up below pH 4.0.

Yet, this does not rule an impact form Cl^-. Therefore, it was deemed relevant to investigate the potential role of Cl^- in these two phenomena.

To that effect, the heats of Na/K and K/Na exchange were measured at pH 2.0 to determine whether moving an extra 1.25 pH units below the PZNC will decrease the measured heats accordingly. Moreover, the heats of Na^+ and K^+ exchange were measured using NO_3^- as the counter-ion instead of Cl^-. These measurements were done at pH 2.0, 3.25, 5.8, and 11.0.

Figure 3.22 displays the representative heat signals of Na/**K** and K/**Na** exchange at pH 2.0 overlain on the signals acquired at pH 3.25. The mass normalized heats of exchange of both reactions are presented in Table 3.9.

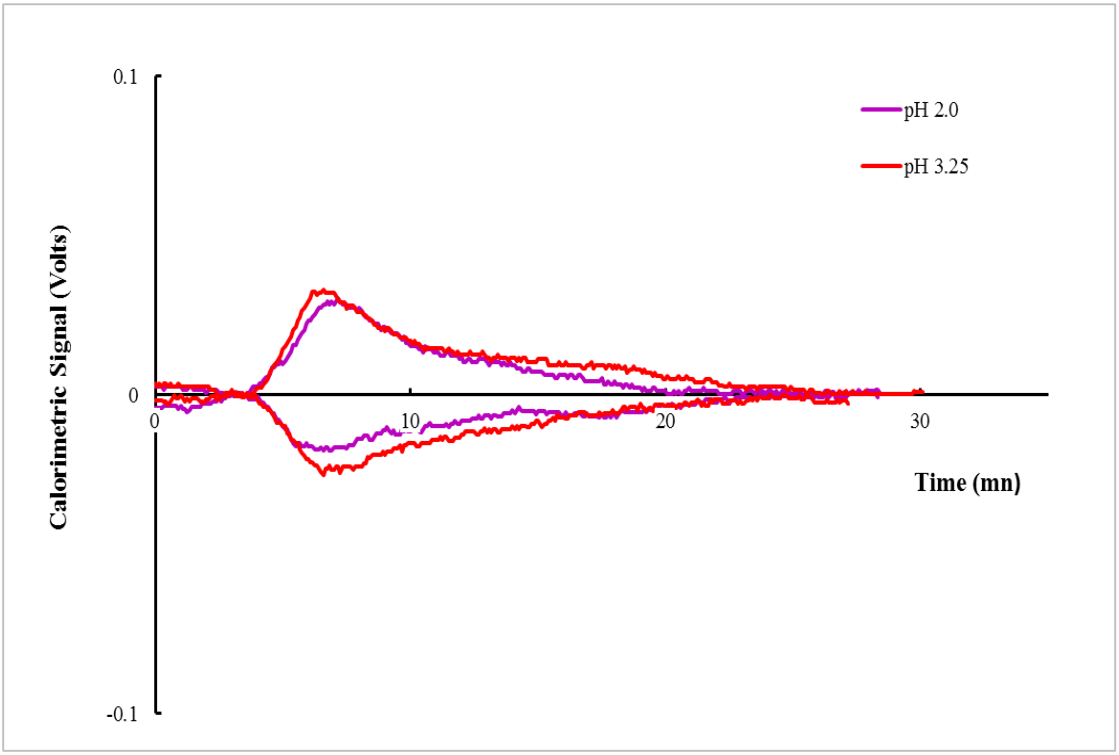

Figure 3.22. Heats Signals of $Na^+$and K^+ Exchange at pH 2.0 and 3.25 in Cl^- on Rutile.

Table 3.9. Heats of Na^+ and K^+ Exchange in Cl^- at pH 2.0 and pH 3.25 on Rutile.

pH	Heat of K/**Na**[a] Exchange (mJ/mg)	K/**Na** Heat Ratio $\frac{\text{pH 2.0}}{\text{pH 3.25}}$	Heat of Na/**K** Exchange (mJ/mg)	Na/**K** Heat Ratio $\frac{\text{pH 2.0}}{\text{pH 3.25}}$
2.0	0.015 (0.001)[b]	0.75	0.032 (0.002)	0.80
3.5	0.020 (0.001)		0.040 (0.002)	

[a] X/**Y**, the exchange of ion X by ion **Y**.
[b] Numbers in parenthesis ( ), ± one standard deviation.

Both Na/**K** and K/**Na** exchanges produced less heat at pH 2.0 than at pH 3.25 on rutile indicating a decrease in the negative surface charge available for cation exchange. Interestingly, the incongruence between the energies of K/**Na** and Na/**K** exchanges persisted with the former lower by *ca.* 50% than the latter.

Table 3.10 lists the heats of Na^+ and K^+ exchange (mJ/mg) with NO_3^- as the counter ion at the four pH values. Figure 3.23 displays the representative raw heat signals at the same pHs.

Table 3.10. Heats of Na^+ and K^+ Exchange in NO_3^- on Rutile

pH	Probe	Calorimetric Heat of Exchange (mJ/mg)	$\frac{\text{K/Na}^c}{\text{Na/K}}$
2	K/**Na**[a]	0.066 (0.002)[b]	1.2
	Na/**K**	0.056 (0.003)	
3.25	K/**Na**	0.077 (0.004)	0.88
	Na/**K**	0.088 (0.005)	
5.8	K/**Na**	0.103 (0.001)	0.66
	Na/**K**	0.156 (0.009)	
11	K/**Na**	0.380 (0.006)	0.79
	Na/**K**	0.408 (0.019)	

[a] X/**Y**, the exchange of ion X by ion **Y**.
[b] Numbers in parenthesis ( ), ± one standard deviation
[c] Ratio of heat (mJ/mg) of K/**Na** exchange to Na/**K** exchange.

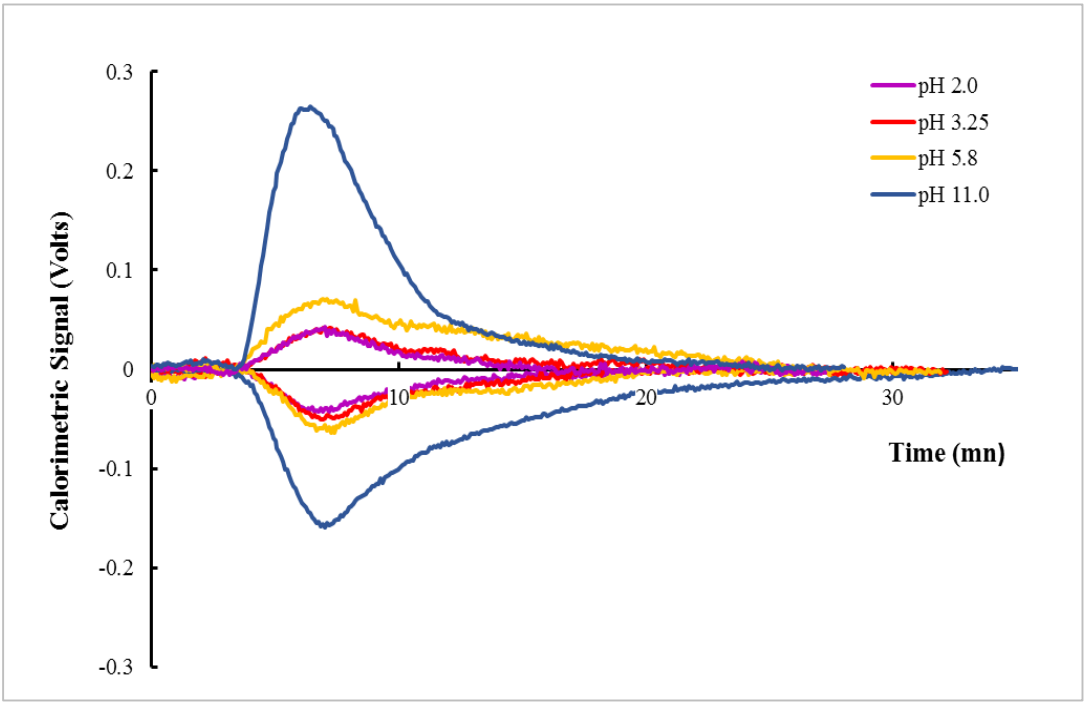

Figure 3.23. Heat Signals of Na^+ and K^+ Exchange in NO_3^- at various pHs on Rutile.

The heats of K/**Na** and Na/**K** exchange produced more heat at pH values near and below the experimental PZNC (i.e. neutral and positive charge conditions) when the background electrolyte species is NO_3^- , which suggests that less negative charge is present in Cl^- at these pH conditions and supports the possibility that Cl^- may be replacing some terminal oxygen sites on rutile at low pH values. However, at pH 11.0 (negative charge) the heats of the cation exchanges in NO_3^- are slightly smaller but still comparable to the heats of exchange in Cl^-. As can be seen from Figure 3.23, the differences in peak size and shape between the Na/**K** and K/**Na** exchanges at pH 3.25 and 2.0 are less pronounced in NO_3^- than they were in Cl^-, where Na/**K** exchange produced approximately 50% more heat than K/**Na** exchanges. At pH 5.8 and 11.0 the differences in the Na/**K** and K/**Na** exchanges correspond to about 65% and 80%, respectively, in both NO_3^- and Cl^-, which lends further support for the possibility of the specific adsorption of Cl^- to a terminal

Ti surface atom at low pHs. The discrepancy between the Na/**K** and K/**Na** exchanges at higher pH regardless of background electrolyte must result from the fact that at neutral and negative conditions the difference in hydration radius and enthalpy of Na^+ and K^+ ions plays a more significant role than the counter ion species.

4 CONCLUSIONS

Flow calorimetry was used to measure the surface charge and PZNC of anatase and rutile. Surface charge is directly proportional to heats of exchange. The flow adsorption microcalorimeter measured heats of CE using Na^+, K^+, and $Rb^{+,}$ and AE using Cl^- and NO_3^-. Measuring theses heats of exchange at various pH values allowed for the determination of the PZC of both polymorphs. For anatase a PZNC of approximately 5.3 was determined, which tended to be slightly lower than those reported in the literature. On rutile, the PZNC depended on the cation species used to measure the negative surface charge. When K/**Na** exchange was used the PZNC was approximately 5.8, whereas when measured using Na/**K** exchange the PZNC was 5.4 which is closer to those values reported in literature. This discrepancy is attributed to the presence of more surface charge on rutile when in Na^+ than when in K^+ due to the dominance of the tetratdentate binding geometry of larger cations (i.e. K^+, Rb^+).

The presence of a significant amount of negative charge at low pHs on rutile was observed. To further investigate the source of the negative charge at the surface the experiment was repeated using cation exchange at pH 2.0. Less heat was measured at pH 2.0 than at pH 3.25 indicating the presence of negatively charged sites on the surface itself, although the role of Cl- could not be ruled out. Additionally, heats of cation exchange on rutile were measured with nitrate as the co-anion instead of chloride since it has been suggested in literature that chloride has an effect on surface charge at low pH values. The magnitude of the heats of cation exchange were larger when measured in nitrate than chloride, which seems to indicate that chloride may indeed replace some terminal water molecules at positive surface charge. Overall, the work highlighted the utility of FAMC data in probing and understanding MO interfacial processes.

REFERENCES

Allmaras, R. R., Gupta, S. C., Kubota, J., Scott, A. D., Smith, S. J., Sparks, D. L., Welch, R. M. (2012). *Advances in Soil Science*: Springer New York.

Appel, C., Ma, L. Q., Rhue, R. D., & Kennelley, E. (2003). Point of zero charge determination in soils and minerals via traditional methods and detection of electroacoustic mobility. *Geoderma, 113*, 77-93.

Appel, C., Rhue, D., Ma, L., & Reve, B. (2002). Heats of K/Ca and K/Pb exchange in two tropical soils as measured by flow calorimetry 1. *Soil science, 167*(12), 773-781.

Bourikas, K., Hiemstra, T., & Van Riemsdijk, W. H. (2001). Ion pair formation and primary charging behavior of titanium oxide (anatase and rutile). *Langmuir, 17*(3), 749-756

Bourikas, K., Kordulis, C., & Lycourghiotis, A. (2014). Titanium Dioxide (Anatase and Rutile): Surface Chemistry, Liquid–Solid Interface Chemistry, and Scientific Synthesis of Supported Catalysts. *Chemical Reviews, 114*(19), 9754-9823. doi: 10.1021/cr300230q

Brown, G. E., Foster, A. L., & Ostergren, J. D. (1999). Mineral surfaces and bioavailability of heavy metals: a molecular-scale perspective. *Proceedings of the National Academy of Sciences, 96*(7), 3388-3395.

Davis, J. A., & Kent, D. (1990). Surface complexation modeling in aqueous geochemistry. *Reviews in Mineralogy and Geochemistry, 23*(1), 177-260.

Essington, M. E. (1994). *Soil-Water Interactions: Mechanisms Applications, Second Edition, Revised Expanded*: Taylor & Francis.

Essington, M. E. (2015). *Soil and water chemistry: An integrative approach*: CRC press.

Fenter, P., Cheng, L., Rihs, S., Machesky, M., Bedzyk, M. J., & Sturchio, N. C. (2000). Electrical double-layer structure at the rutile–water interface as observed in situ with small-period X-ray standing waves. *Journal of Colloid and Interface Science*, *225*(1), 154-165.

Ferreira, D. R., Schulthess, C. P., & Kabengi, N. J. (2013). Calorimetric Evidence in Support of the Nanopore Inner Sphere Enhancement Theory on Cation Adsorption. *Soil Science Society of America Journal, 77*(1), 94-99.

Gale, S. A., Harvey, O. R., & Rhue, R. D. (2015). Phosphate alteration of chloride behavior at the boehmite–water interface: New insights from ion-probe flow adsorption microcalorimetry. *Journal of Colloid and Interface Science*, *455*, 71-77.

Goldberg, S. (2014). Application of surface complexation models to anion adsorption by natural materials. *Environmental Toxicology and Chemistry, 33*(10), 2172-2180.

Goldberg, S., Criscenti, L. J., Turner, D. R., Davis, J. A., & Cantrell, K. J. (2007). Adsorption–desorption processes in subsurface reactive transport modeling. *Vadose Zone Journal, 6*(3), 407-435.

Goldberg, S., & Sposito, G. (1985). On the mechanism of specific phosphate adsorption by hydroxylated mineral surfaces: A review. *Communications in Soil Science & Plant Analysis, 16*(8), 801-821.

Goulding, K., & Talibudeen, O. (1984). Thermodynamics of K-Ca exchange in soils. *Journal of soil science, 35*(3), 397-408.

Guichet, X., Jouniaux, L., & Catel, N. (2006). Modification of streaming potential by precipitation of calcite in a sand–water system: laboratory measurements in the pH range from 4 to 12. *Geophysical Journal International*, *166*(1), 445-460.

Hiemstra, T., & Van Riemsdijk, W. H. (1996). A surface structural approach to ion adsorption: the charge distribution (CD) model. *Journal of Colloid and Interface Science, 179*(2), 488-508.

Hiemstra, T., Van Riemsdijk, W. H., & Bolt, G. H. (1989). Multisite proton adsorption modeling at the solid/solution interface of (hydr) oxides: A new approach: I. Model description and evaluation of intrinsic reaction constants. *Journal of colloid and interface science, 133*(1), 91-104.

Hiemstra, T., Yong, H., & Van Riemsdijk, W. H. (1999). Interfacial charging phenomena of aluminum (hydr) oxides. *Langmuir, 15*(18), 5942-5955.

Holmberg, J. P., Ahlberg, E., Bergenholtz, J., Hassellöv, M., & Abbas, Z. (2013). Surface charge and interfacial potential of titanium dioxide nanoparticles: Experimental and theoretical investigations. *Journal of Colloid and Interface Science, 407*, 168-176. doi: http://dx.doi.org/10.1016/j.jcis.2013.06.015

Hunter, R. J. (1981). *Zeta potential in colloid science: principles and applications*. London a.o: Academic Press.

Ibanez, J. G., Hernandez-Esparza, M., Doria-Serrano, C., Fregoso-Infante, A., & Singh, M. M. (2008). The Point of Zero Charge of Oxides. *Environmental Chemistry* (pp. 70-78): Springer.

Kabengi, N. J. (2004). *Measuring surface chemical properties using flow adsorption calorimetry: The case of amorphous aluminum hydroxides and arsenic (V).* University of Florida.

Kabengi, N., Daroub, S. H., Rhue, R. D. (2006). Energetics of Arsenate Sorption on Amorphous Aluminum Hydroxides Studied Using Flow Adsorption Calorimetry. *Journal of Colloid and Interface Science, 297*, 86-94.

Kabengi, N., Rhue, R. D and Daroub, S. H. (2006). Using flow calorimetry to determine the molar heats of cation and anion exchange and the point of zero net charge (PZNC) on amorphous aluminum hydroxides. *Soil Science, 171*, 13-20.

Kenichi, U., Kei, K., Noriaki, O., Kazumi, M., & Hirofumi, Y. (2015). Molecular-scale quantitative charge density measurement of biological molecule by frequency modulation atomic force microscopy in aqueous solutions. *Nanotechnology*, *26*(28), 285103.

Kosmulski, M. (2009). pH-dependent surface charging and points of zero charge. IV. Update and new approach. *Journal of Colloid and Interface Science, 337*(2), 439-448.

Lützenkirchen, J., Preočanin, T., Kovačević, D., Tomišić, V., Lövgren, L., & Kallay, N. (2012). Potentiometric titrations as a tool for surface charge determination. *Croatica Chemica Acta*, *85*(4), 391-417.

Lützenkirchen-Hecht, D., & Strehblow, H.-H. (1998). Surface analytical investigations of the electrochemical double layer on silver electrodes in alkaline media. *Electrochimica acta, 43*(19), 2957-2968.

Machesky, M. L., Andrade, W. O., & Rose, A. W. (1991). Adsorption of gold (III)-chloride and gold (I)-thiosulfate anions by goethite. *Geochimica et Cosmochimica Acta, 55*(3), 769-776.

Machesky, M. L., & Jacobs, P. F. (1991a). Titration calorimetry of aqueous alumina suspensions Part I. Results and comparison with similar studies. *Colloids and Surfaces, 53*(2), 297-314.

Machesky, M. L., & Jacobs, P. F. (1991b). Titration calorimetry of aqueous alumina suspensions part II. Discussion of enthalpy changes with pH and ionic strength. *Colloids and Surfaces, 53*(2), 315-328.

Machesky, M. L., Palmer, D. A., & Wesolowski, D. J. (1994). Hydrogen ion adsorption at the rutile-water interface to 250 C. *Geochimica et Cosmochimica Acta, 58*(24), 5627-5632.

Machesky, M. L., Wesolowski, D. J., Palmer, D. A., Ridley, M. K., Bénézeth, P., Lvov, S. N., & Fedkin, M. V. (2006). Chapter 12 Ion adsorption into the hydrothermal regime: experimental and modeling approaches. *Interface Science and Technology, 11*(C), 324-358. DOI: 10.1016/S1573-4285(06)80056-6

Machesky, M. L., Předota, M., Ridley, M. K., & Wesolowski, D. J. (2015). Constrained Surface Complexation Modeling: Rutile in RbCl, NaCl, and NaCF3SO3 Media to 250 °C. *The Journal of Physical Chemistry C, 119*(27), 15204-15215. doi: 10.1021/acs.jpcc.5b02841

Marcano-Martinez, E., & McBride, M. B. (1989). Comparison of the titration and ion adsorption methods for surface charge measurement in Oxisols. *Soil Science Society of America Journal, 53*(4), 1040-1045.

McBride, M. B. (1994). *Environmental chemistry of soils*: Oxford university press.

Moghimi, A. H., Hamdan, J., Shamshuddin, J., Samsuri, A. W., & Abtahi, A. (2013). Physicochemical Properties and Surface Charge Characteristics of Arid Soils in Southeastern Iran. *Applied and Environmental Soil Science, 2013*, 11. doi: 10.1155/2013/252861

Myers, D. (1990). *Surfaces, interfaces and colloids*: Wiley-Vch New York etc..

Panagiotou, G. D., Petsi, T., Bourikas, K., Garoufalis, C. S., Tsevis, A., Spanos, N., Lycourghiotis, A. (2008). Mapping the surface (hydr) oxo-groups of titanium oxide and

its interface with an aqueous solution: the state of the art and a new approach. *Advances in colloid and interface science, 142*(1), 20-42.

Parker, J. C., Zelazny, L. W., Sampath, S., & Harris, W. G. (1979). A critical evaluation of the extension of zero point of charge (ZPC) theory to soil systems. *Soil Science Society of America Journal, 43*(4), 668-674.

Predota, M., Bandura, A., Cummings, P., Kubicki, J., Wesolowski, D., Chialvo, A., & Machesky, M. (2004). Electric double layer at the rutile (110) surface. 1. Structure of surfaces and interfacial water from molecular dynamics by use of ab initio potentials. *The Journal of Physical Chemistry B, 108*(32), 12049-12060.

Ramprasad, R., Hass, K. C., Schneider, W. F., & Adams, J. B. (1997). Cu−Dinitrosyl Species in Zeolites: A Density Functional Molecular Cluster Study. *The Journal of Physical Chemistry B, 101*(35), 6903-6913. doi: 10.1021/jp962706e

Rhue, R. D., Appel, C., & Kabengi, N. (2002). Measuring surface chemical properties of soil using flow calorimetry 1. *Soil science, 167*(12), 782-790.

Ridley M. K., Hackley V. A. and Machesky M. L. (2006) Characterization and surface-reactivity of nanocrystalline anatase in aqueous solutions. *Langmuir* 22, 10972–10982.

Ridley, M. K., Hiemstra, T., van Riemsdijk, W. H., & Machesky, M. L. (2009). Inner-sphere complexation of cations at the rutile–water interface: A concise surface structural interpretation with the CD and MUSIC model. *Geochimica et Cosmochimica Acta, 73*(7), 1841-1856. doi: http://dx.doi.org/10.1016/j.gca.2009.01.004

Ridley, M. K., Machesky, M. L., & Kubicki, J. D. (2013). Anatase Nanoparticle Surface Reactivity in NaCl Media: A CD–MUSIC Model Interpretation of Combined

Experimental and Density Functional Theory Studies. *Langmuir, 29*(27), 8572-8583. doi:10.1021/la4011955

Rudziński, W., Panas, G., Charmas, R., Kallay, N., Preočanin, T., & Piasecki, W. (2000). A Combined Temperature−Calorimetric Study of Ion Adsorption at the Hematite−Electrolyte Interface: I. Model of a Homogeneous Oxide Surface. *The Journal of Physical Chemistry B, 104*(50), 11912-11922. doi: 10.1021/jp001311z

Sabur, M. A., Goldberg, S., Gale, A., Kabengi, N., & Al-Abadleh, H. A. (2015). Temperature-dependent infrared and calorimetric studies on arsenicals adsorption from solution to hematite nanoparticles. *Langmuir, 31*(9), 2749-2760.

Selim, H. M., & Zhang, H. (2013). Modeling approaches of competitive sorption and transport of trace metals and metalloids in soils: a review. *J Environ Qual, 42*(3), 640-653. doi: 10.2134/jeq2012.0323

Smith, K. S. (1999). Metal sorption on mineral surfaces: an overview with examples relating to mineral deposits. *The Environmental Geochemistry of Mineral Deposits. Part A: Processes, Techniques, and Health Issues, 6*, 161-182.

Sparks, D. L. (2001). Elucidating the fundamental chemistry of soils: past and recent achievements and future frontiers. *Developments and Trends in Soil Science, 100*(3–4), 303–319. doi:10.1016/S0016-7061(01)00026-X

Sparks, D. L. (2003). *Environmental Soil Chemistry*: Academic Press.

Sposito, G. (1981). *The thermodynamics of soil solutions*: Oxford University Press.

Sposito, G. (2008). *The Chemistry of Soils*: Oxford University Press.

Sverjensky, D. A. (1994). Zero-point-of-charge prediction from crystal chemistry and solvation theory. *Geochimica et Cosmochimica Acta, 58*(14), 3123-3129. doi: http://dx.doi.org/10.1016/0016-7037(94)90184-8

Tadanier, C.J. and M.J. Eick. 2002. Formulating the charge-distribution multisite surface complexation model using FITEQL. *Soil Science Society of America* 66:1505-1517.

Tombácz, E. (2009). pH-dependent surface charging of metal oxides. *Periodica Polytechnica.Chemical Engineering, 53*(2), 77-86. doi: http://dx.doi.org/10.3311/pp.ch.2009-2.0

Van Raij, B., & Peech, M. (1972). Electrochemical properties of some Oxisols and Alfisols of the tropics. *Soil Science Society of America Journal, 36*(4), 587-593.

Vohs, J. M. (2013). Site Requirements for the Adsorption and Reaction of Oxygenates on Metal Oxide Surfaces. *Chemical Reviews, 113*(6), 4136-4163. doi: 10.1021/cr300328u

Wesolowski, D. J., Machesky, M. L., Ridley, M. K., Palmer, D. A., Zhang, Z., Fenter, P., Cummings, P. T. (2008). Ion adsorption on metal oxide surfaces to hydrothermal conditions. In *ECS Transactions - Interfacial Electrochemistry and Chemistry in High Temperature Media*, *27*(11), 167-180. doi: 10.1149/1.2939086

Westall, J., and Hohl, H. (1980). A comparison of electrostatic models for the oxide/solution interface. *Adv. in Colloid Interface Sci*, *12*, 265–294.

Wypych, A., Bobowska, I., Tracz, M., Opasinska, A., Kadlubowski, S., Krzywania-Kaliszewska, A., . . . Wojciechowski, P. (2014). Dielectric Properties and Characterisation of Titanium Dioxide Obtained by Different Chemistry Methods. *Journal of Nanomaterials, 2014*, 9. doi: 10.1155/2014/124814

Zhang, X.-J., Ma, T.-Y., & Yuan, Z.-Y. (2008). Titania-phosphonate hybrid porous materials: preparation, photocatalytic activity and heavy metal ion adsorption. *Journal of Materials Chemistry, 18*(17), 2003-2010. doi: 10.1039/B717060B

Zhang, Z., Fenter, P., Cheng, L., Sturchio, N. C., Bedzyk, M. J., Předota, M., . . . Wesolowski, D. J. (2004). Ion Adsorption at the Rutile−Water Interface: Linking Molecular and Macroscopic Properties. *Langmuir, 20*(12), 4954-4969. doi: 10.1021/la0353834